A comprehensive study of the liquid transfer from the front to the back of a vertical perforated sheet

Manasa Iyer, Joel Casalinho, John Pachón-Morales, Jacopo Seiwert, Mikael Wattiau, Laurent Zimmer, Hervé Duval

A comprehensive study of the liquid transfer from the front to the back of a vertical perforated sheet

Manasa IYER[1,3], Joel CASALINHO[1], John PACHON[3], Jacopo SEIWERT[3], Mikael WATTIAU[3], Laurent ZIMMER[2], Hervé DUVAL[1*],

1 Université Paris-Saclay, CentraleSupélec, Laboratoire de Génie des Procédés et Matériaux, F-91190 Gif-sur-Yvette, France

2 Université Paris Saclay, CentraleSupelec, CNRS, Laboratoire EM2C, F-91190 Gif-sur-Yvette, France

3 Campus Innovation Paris, Air Liquide Research & Development, 1, chemin de la Porte des Loges, 78350 Les Loges-en-Josas, France

***Corresponding author**

Abstract:

Perforations contribute to liquid redistribution in corrugated sheet packings. We focus on a simplified but relevant experimental configuration where a vertical perforated flat sheet is solely supplied with liquid on its front. We then examine how the perforations irrigate the back of the plate when operating in the liquid curtain mode. We successively consider a single perforation, a spanwise row of perforations, and a staggered array of perforations.

We quantify the liquid transfer through the perforations as a function of the supply flow rate, and we explore the effects of perforation diameter, perforation spacing, and plate thickness. We also analyze the spreading of the rivulets leaking from the perforations, their merging into a continuous wavy film, and the leveling of this film as it falls down the plate. The spreading and the merging exhibit a power-law behavior in agreement with theoretical models. The leveling exhibit exponential decay behavior.

Topical Heading: Transport Phenomena and Fluid Mechanics

Key Words: Structured packing, liquid film, liquid curtain, rivulet, spreading, film leveling

Introduction

Corrugated sheet packings are well suited for low liquid and vapor load applications, where minimizing column pressure drop is essential. Since their successful application in the early 80s, these packings have become predominant in cryogenic air separation. Corrugated sheet packings consist of metallic crimped sheets placed vertically, side by side, with the corrugations of adjacent sheets crisscrossing one another. Such packings combine a high void fraction and a high interfacial area, resulting in a lower pressure drop and a higher capacity than trays or random packings at the same efficiency. However, the separation performances of corrugated sheet packings are very sensitive to the uniformity of liquid distribution over the column cross-section compared to random packings. Indeed, in corrugated sheet packings, the vapor flow cannot redistribute the liquid over the column cross-section as apparatuses with random packings operating near the flooding point. The addition of perforations that transfer liquid from one side of a sheet to another decreases the sensitivity of corrugated sheet packings to irrigation uniformity[1].

As the liquid phase is poured to the top of the packing, liquid spreading throughout the packing essentially depends on the packing geometry[2], the liquid flow rate[6], the liquid viscosity[6], and the contact angle of the liquid on the sheets[3,4]. Liquid distribution further conditions the liquid hold-up, the liquid-vapor interfacial area, and the mass transfer within the packing.

Three geometrical features contribute to liquid distribution: the corrugations, the perforations, and optionally the microtexture of the sheets. Whereas the liquid tends to flow vertically from the pour points, the troughs of the corrugated sheets guide the liquid in the transverse direction

of the sheets. The contact points between the corrugations of adjacent sheets divide the liquid flow between the sheets. The perforations transfer the liquid from one side of a sheet to the other side. Last, the microtexture enhances the wettability of the sheets.

Liquid distribution and spreading over corrugated sheet packings have been investigated at different scales: (pilot) column scale, sheet scale, and geometrical feature scale.

Tomographic techniques are efficient, non-intrusive tools to view inside a packed column and analyze the liquid flow distribution at the column scale. Fourati et al.[2] used gamma-ray tomography to investigate liquid distribution in a counter-current gas-liquid column equipped with Mellapack 250.X packing and fed with a central liquid jet at the top. The working liquids were water and MEA 30wt%. They obtained hold-up maps (expressed in liquid volume fraction) at different axial positions in the column. They found that the overall liquid hold-up increases with the liquid flow rate and the liquid viscosity. The liquid phase disperses radially with a spreading factor[5] of the order of a few millimeters. Since the spreading factor does not significantly vary with the liquid load, the gas load, and the liquid viscosity, Fourati et al.[2] conclude that liquid distribution is mainly controlled by the packing geometry.

Most of the 3-D images of the packed column inside have been obtained using X-ray computed tomography (XCT)[6,7,8]. Janzen et al.[6] investigated the liquid flow morphology in a small column equipped with MellapakPlus 752.Y packing and fed either with pure water or water-glycerin mixtures. They found that the overall liquid hold-up and the gas-liquid interfacial area increase with the liquid load and the liquid viscosity. They distinguish three flow patterns: film flow, liquid menisci/bridges at the contact points between corrugations of adjacent sheets, and flooded regions. The relative contribution of the film-flow pattern to hold-up decreases with both the liquid load and the liquid viscosity, while the relative contribution of the flooded regions increases correspondingly. The contribution of the liquid menisci appears independent of the varied parameters. Schug & Arlt[7] imaged the liquid flow morphology in different

Mellapak 500.Y packings, i.e., with smooth, fluted, and gridded microtexture, with or without perforations. Packings were irrigated with water. The liquid hold-up in the packing with the gridded texture and holes shows the highest values, and the results indicate that the more complex the surface modification is, the higher is the liquid hold-up. The evaluation of the liquid film thickness shows that the packings are not totally wetted. Dry areas (or covered by a film below the resolution limit) subsist even at high liquid loads. Most of the liquid is located in the troughs of the sheets in the form of rivulets, and at the contact points between sheets in the form of liquid bridges. Wehrli et al.[8] examined liquid flow in Mellapak 250.Y and Mellapak 500.Y packings fed either with water or propan-2-ol. They found that the packings are better wetted by propan-2-ol than by water. They also distinguish three patterns, i.e., liquid films, rivulets, and bridges. Water tends to form rivulets in the troughs and bridges at the contact points, while a significant fraction of the packing surface remains not covered. Propan-2-ol tends to form liquid films that cover the packing surface uniformly.

Liquid distribution mechanisms have been investigated with experiments carried out on a single corrugated sheet. The sheet is placed vertically and supplied with liquid on one side only. Either one or several channels (i.e., troughs) on the upper edge of the corrugated sheet are irrigated. For X and Y packings, it is found that the liquid flow pattern and the subsequent wetted area depend on the corrugation angle, surface microtexture, perforations, and flow parameters[9–11]. We retain that the wetted surface area increases with the liquid flow rate. Below a minimum film Reynolds number ($\mathrm{Re} \cong 100$ for liquid nitrogen), the liquid cannot cross the channel crests. It flows along the valley of the irrigated channel and does not fall into the underlying (non-irrigated) channels. The transferred flow through the perforations (from the supplied side to the non-supplied one) also depends on the local liquid flow rate and their position on the channel surface (flank, crest, or valley). The liquid is only transferred above a minimum film Reynolds number ($\mathrm{Re} \cong 100 - 160$). Then, the transferred flow rate increases with the local

liquid flow rate (on the front of the plate, just upstream of the hole). Perforations may also facilitate the liquid flow from a channel to the underlying ones by multiple transfers, i.e., from the supplied side of the plate to the opposite one and back. We stress that the interplay between the inclined corrugations and the perforations makes the analysis very difficult. Gorodilov et al.[1] quantified the transferred flow rate from the supplied side (front) to the non-supplied side (back) of a corrugated plate perforated with slits (instead of the standard round perforations). Corrugations and slits were parallel to the horizontal plane. The working liquid was water. They found that the liquid transfer starts above a minimum film Reynolds number and exhibits a hysteresis loop when varying the supply flow rate at the upper edge of the corrugated sheet. The threshold and the hysteresis loop are attributed to the liquid meniscus blockage at the slit entrance.

Studies focusing on a single geometrical feature (perforation or channel, for example) provide helpful insight into the elementary mechanisms involved in packed column. Xie et al.[12,13] and Iyer et al.[14] considered the liquid flow down a vertical plate with a single perforation, round[14] or rectangular[12,13]. The plate was supplied with liquid either on one or two sides. At low values of the film Reynolds number, the liquid film flow is deflected by the perforation, and the liquid does not fill the perforation. Above a critical value of the Reynolds number, referred to as the curtain Reynolds number, the liquid fills the perforation entirely and forms a liquid curtain. Xie et al.[12,13] and Iyer et al. [14] further investigated the curtain regime when the plate is supplied with equal volume flow rate on its front and on its back. The varicose capillary waves standing on the liquid curtain and the strong vorticity generation both inside the curtain and on its free surface explain the mass transfer intensification observed for the plate with perforation (as compared to the unperforated plate)[15]. However, the authors did not examine the effects of perforation on liquid redistribution.

Shetty & Cerro[16] investigated the spreading of a rivulet over an inclined flat solid surface. Such a simplified configuration typically mimics the rivulet flowing in a channel of a corrugated sheet. Experiments were performed with silicone oils of two different viscosities and a brass plate at a varying inclination angle. The plate was fed at a single drip point by a small liquid jet. They observed that the rivulet spanwise profile evolves self-similarly and is well represented by a Gaussian. They used a viscous long-wave approximation to derive a film evolution equation and obtain the scaling laws followed by the rivulet. They distinguished two spreading regimes, i.e., capillary-dominant and gravity-dominant. When the capillarity (resp. gravity) controls the spreading, the spanwise spreading follows the $3/13^{th}$ (resp. $3/7^{th}$) power of the distance traveled along with the flow (with appropriate rescaling) while the rivulet peak thickness thins out as the -1/13 (resp. -1/7) power of the traveled distance. They found a good agreement between the theory and the experiments. For an angle of inclination to the vertical greater than 10°, the spreading is controlled by gravity. It should be noted that the scaling laws for the gravity-dominant regime were first obtained by Smith[17], who derived a similarity solution for a viscous source flow down an inclined plane. Duffy & Moffatt[18,19] later obtained a similarity solution for a viscous source flow down a vertical plane and recovered the exponents of the capillary-dominant regime first found by Shetty & Cerro[16].

To better understand how the perforations contribute to liquid distribution in corrugated sheet packings, we consider a simplified configuration where a vertical perforated flat sheet is solely supplied with liquid on its front. We examine how the perforations irrigate the back of the plate. Plates have either a single perforation, a spanwise row of perforations, or a staggered array of perforations. We quantify the liquid transfer through the perforations as a function of the supply flow rate. After examining the impact of the flow regime on the transfer, we further focus on the curtain regime. We explore the effects of the perforation diameter, the perforation spacing, and the plate thickness. We carefully analyze the spreading of the rivulets leaking on the back

of the plate from the perforations, the merging of the rivulets into a continuous film, and the leveling of this film as it falls down the plate. Liquid film thickness profiles are assessed using confocal chromatic imaging.

In the first part of the paper, we briefly address the physics of the problem. In the second part, we describe our experimental setup and the associated measurement methods. The third part presents our experimental data. The fourth part discusses the results and compares them to models either found in the literature or newly developed.

Problem description

We consider a vertical flat plate or sheet of thickness t with single or multiple circular perforations of diameter d (Figure 1). The plate is supplied with liquid on its front, above the first row of perforations. We study the liquid transfer from the front to the back of the plate. x denotes the streamwise direction, y the spanwise direction, and z is the direction in the thickness of the liquid film. Three perforation patterns are examined: (i) single perforation, (ii) spanwise row of equally-spaced perforations, and (iii) staggered array of perforations. s is the (centre-to-centre) spacing between the perforations in y-direction as well as the pitch (in x-direction) between the rows of perforations (see Figure 1).

We consider a Newtonian liquid with constant physical properties such as density (ρ), kinematic viscosity (ν) and surface tension (σ). $\mu = \rho\nu$ is its dynamic viscosity. We suppose that the equilibrium contact angle (θ_E) of the liquid on the plate is significantly lower than $\pi/2$. Then, wetting is favorable.

The front of the plate is supplied with liquid at a volume flow rate q. We define Q the supply flowrate per unit width, i.e., $Q = q/w$, where w is the width of the channel bounded by the frame that holds the plate (see Figure 1). The flow upstream of the perforations is characterized by the film Reynolds number which compares the inertial forces with the viscous forces acting on the film, i.e., $\mathrm{Re} = Q/\nu$. Thereafter, Re will be referred to as the supply Reynolds number.

We assume that the film flow upstream of the perforations is steady, laminar and fully developed. We suppose that the amplitude of the waves that may travel on the free surface remains much lower than the film thickness. Then, the upstream film thickness is well described by the Nusselt[20] thickness, $\delta_{Nu}(Q) = (3\nu Q/g)^{1/3}$.

For a single perforation or a single spanwise row of perforations, we note q_t the total volume flow rate transferred through the perforations. In the absence of supply on the back of the plate, q_t coincides with the volume flow rate q_b flowing on the back of the plate beneath the perforations. We define the transferred volume flow rate per unit diameter of perforation $Q_t = q_t/(Nd)$ with N the number of perforations. Following Gorodilov et al.[1], we also introduce the so-called overflow number $X = Q_t/Q$ which quantifies the liquid transfer efficiency of a perforation.

For a staggered array of perforation, we index the rows from top ($k = 1$) to bottom ($k = n$). N is the number of perforations of the odd numbered rows, $(N - 1)$ the number of perforations of the even. The width of the array is defined as $w_a = Ns$. We note $q_b(k)$ the volume flow rate on the back of the plate just beneath the kth row of perforations. The volume flow rate per unit width on the back of the plate just beneath the kth row of perforations is defined as $Q_b(k) = q_b(k)/w_a$.

Last, we define $\delta(x, y)$ the local thickness of the liquid film on the back of the plate.

When a liquid film flows over a single perforation of small diameter ($d \leq 8$ mm), different regimes may be distinguished depending on (1) the value of the film Reynolds number and (2) the history of the film flow[14]. When Re is low, the film flow is deflected by the perforation and does not fill it. The contact line is pinned at the top edge of the perforation (front of the plate) and there is no fluid transfer from the front to the back of the plate. When Re is moderate, a liquid rim forms within the perforation and liquid is transferred from the front to the back of the plate. On the back, the liquid climbs over the top edge of the perforation and makes an arch-

shaped capillary ridge that extends in the form of two parallel rivulets (see Figure S1 in Supplementary Material). Therafter, this regime will be referred to as the rim mode. When Re is high, a liquid curtain closes the perforation. Liquid is still transferred from the front to the back of the plate but the flow pattern on the rear side differs from that encountered in the rim mode: the liquid leaks from the bottom edge of the perforation in the form of a single rivulet (see Figure S1 in Supplementary Material). The curtain transition occurs when the inertia of the film balances the surface tension forces. We note Q_{cr} the supply flow rate per unit width at the curtain transition. The curtain Reynolds number Re_{cr} is the Reynolds number associated with Q_{cr}. This regime will be referred to as the inertial curtain mode.

When the supply flow rate is decreased from the inertial curtain mode, the film flow remains in the curtain mode for Re values much lower than Re_{cr}. Liquid is transferred from the front to the back of the plate with the same flow pattern as for $\mathrm{Re} > \mathrm{Re}_{cr}$. This regime will be referred to as the hysteretic curtain mode. This mode is metastable: if a hole is made in the curtain, the film flow switches in the rim mode.

In the rest of the paper, we investigate the effect of perforation diameter (d), perforation spacing (s), plate thickness (t), supply flow rate per unit width (Q) and flow mode (rim, inertial curtain, hysteretic curtain) on (i) the transferred flow rate per unit diameter of perforation (Q_t) and (ii) the subsequent wetting of the back of the plate (by measuring the liquid film profile).

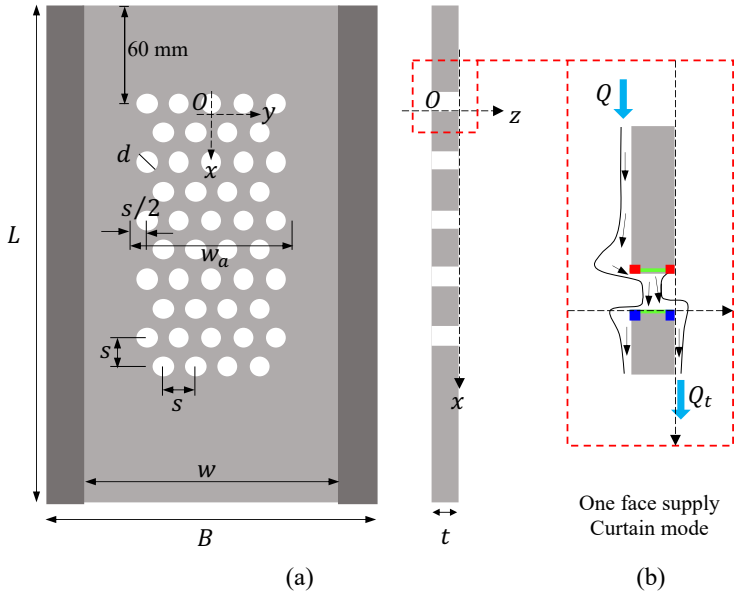

Figure 1. Perforated plate front view and cross-section along x-z plane: (a) geometric parameters and coordinate system (b) Scheme of the film flow on the front and on the back of the plate (the plate is supplied solely on its front, the film flows in the curtain mode). The arrows indicate the flow path followed by the fluid. We define the top edges of the perforation on the front and on the back of the plate (red squares), the bottom edges (blue squares) and the perforation inner surface (in green).

Experimental set-up

Materials

The test plates are cut from aluminum sheets. The plate length in the streamwise direction is $L = 200$ mm and the plate width in the spanwise direction is $B = 150$ mm (see Figure 1).

For the single perforation pattern, two different plate thicknesses, i.e., $t = 0.5$ and 1 mm, and up to six perforation diameters, i.e., $d = 4$, 6, 8, 10, 14 and 16 mm, are considered. We define $d = 4$ mm and $t = 1$ mm as our reference case. The center of the perforation is located on the midline of the plate, at 60 mm from the top edge.

For the single spanwise row of perforations, the plate thickness is $t = 1$ mm, the perforation diameter $d = 4$ mm. Five centre-to-centre spacing, i.e., $s = 6$, 8, 10, 12 and 14 mm are

examined. For each spacing, the number N of perforations is such that $N \times s \leq 70$ mm and N maximal. N is equal to 11, 9, 7, 5 and 5, respectively. Perforations are spread within 70 mm and not within the channel width $w = 90$ mm to reduce side wall effects (the film flow is laterally bounded by the frame that holds the plate).

For the staggered array of perforations (with 2, 3 or 10 rows of perforations), we selected $t = 1$ mm, $d = 4$ mm, and $s = 14$ mm. The pitch between the rows is fixed to $s = 14$ mm.

The test plates are slightly polished with abrasive (grit size P1200) to get a matt rendering and then reduce the impact of light parasitic reflection on optical based measurements. The resulting roughness parameter (Ra, arithmetical average of the roughness profile) of the plate ranges from 0.2 to 0.5 μm with the standard deviation of the order of 0.01 μm as measured by confocal chromatic imaging (3D Measuring Station with CHR 150-N sensor, STIL).

Pure propan-2-ol, purchased from VWR Chemicals (GPR Rectapur® >99.0%), is used as a test liquid. Its physical properties are reported in Table 1 (see Supplementary Material). We stress that the wetting of the aluminum sheets with propan-2-ol is highly favorable ($\theta_E \ll 90°$).

Experimental set-up

Since the setup has already been presented in detail elsewhere, we will only recall its main features. It comprises three parts (see Figure 2): the frame that holds the perforated plate, the liquid circuit, and the instrumentation dedicated to liquid film observation and measurement. The perforated plate is inserted in a rigid frame to ensure its flatness. The frame is held vertically. It is decoupled from the other parts of the device and mounted on an anti-vibration table to damp the parasitic vibrations that may affect the fluid film flowing on the plate. The front of the plate is supplied with liquid by a distributor (carefully designed to uniformly distribute the liquid in the spanwise direction of the plate). The liquid circulates thanks to a magnet gear pump (MDG-M15T3B, Iwaki). The volumetric flow rate delivered by the distributor is set by a needle control valve and monitored by an oval gear volumetric flow meter

(MX06, MacNaught). The liquid flowing from the bottom of the plate comes into a collector and then returns to the feeding tank.

The liquid flow pattern is observed and recorded using a CMOS high-speed camera (v310, Phantom) mounted with a macro lens (AF Zoom-Micro Nikkor 70-180mm f/4.5-5.6D ED, Nikon). Images are captured with a resolution of 1200×800 px² and with an acquisition frequency of 1.8 kHz. For shadowgraph imaging of the suspended film, the plate is illuminated with a LED panel (see Figure 2). When looking at the free surface of the supported film, the plate is lit by a cold light illuminator (KL 2500 LCD, Schott).

The instantaneous local thickness of the liquid film is measured along with the streamwise and spanwise directions using confocal chromatic imaging (sensor CL4, STIL) with a precision better than 0.5 µm at an acquisition frequency of 5 kHz.

The volume flow rate of liquid transferred by the perforations is measured by diverting the liquid flow through a removable collector attached to the back of the plate (see Figure 2). The removable collector is glued at 10 to 15 mm distance from the last row of perforations with blue silicone gasket sealant. The volume flow rate is determined by weighing the diverted liquid.

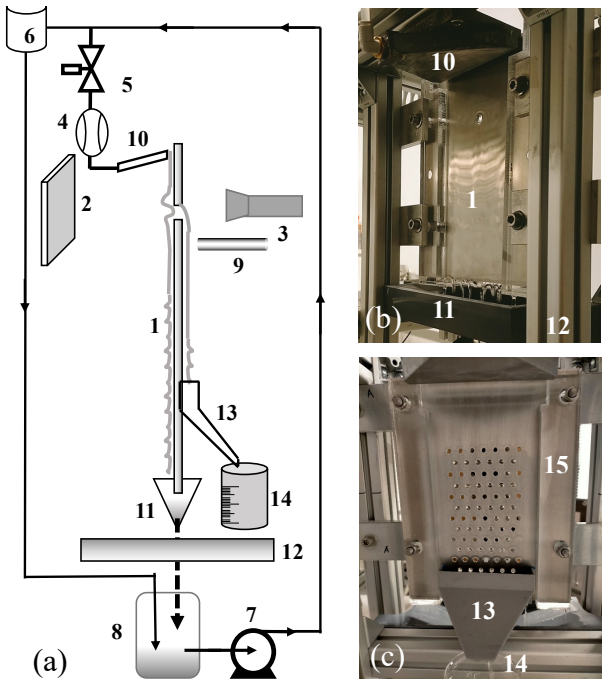

Figure 2. (a) Schematic representation of the experimental set-up. (b) Photograph of the front of the plate (with a single perforation). (c) Photograph of the back (with a staggered array of perforations). 1. Test plate 2. LED panel 3. High-speed camera 4. Volumetric flow meter 5. Needle control valve 6. Spillway 7. Gear pump 8. Reservoir 9. CCI sensor 10. Distributor 11. Liquid Collector 12. Anti-vibration mount, 13. Removable collector, 14. Measuring beaker. 15. Frame that holds the plate.

Experimental protocol

First, the test plate is cleaned with a surfactant solution (3 vol%, Mucasol, Merz), thoroughly rinsed with distilled water and dried with compressed air. Then, the plate is inserted and fixed in the vertical frame. The outlet of the distributor is positioned on the front of the plate about two millimeters below its top edge. Since the outlet is located 60 mm upstream of the first row of perforations, we expect that the film flow would be fully developed on the front side at the location of the perforations. We are aware that a liquid film falling on a vertical flat plate is unconditionally unstable. However, we checked that the amplitude of the waves travelling on the liquid film upstream of the perforations remains small compared to the film thickness. The distance (in z direction) between the distributor nozzles and the plate is carefully adjusted in order to obtain a uniform film thickness in the spanwise (y) direction. The front of the plate is fed with the highest flow rate, i.e., 38 L h^{-1}, such that the liquid is forced to wet the whole usable width of the front side, i.e., $w = 90$ mm. Then, the liquid flowrate can be reduced down to 5 L h^{-1} and the region upstream of the perforations remains totally covered by the liquid film.

The supply flow rate (q) is incrementally swept from 5 L h^{-1} to 38 L h^{-1} and then down to 5 L h^{-1} to explore the rim mode, the inertial curtain mode, and the hysteretic curtain mode successively. We examine if some liquid is transferred through the perforations for each flow rate value (in the forward and backward sweep). We determine the volume flow rate on the back of the plate beneath the perforations (q_b) by measuring the weight of fluid recovered from

the removable collector over a while. We remind that in the absence of supply on the back of the plate, q_t (transferred by a single perforation or a single row of perforations) coincides with q_b just beneath the perforations. Optionally, the topography of the liquid film on the backside of the plate is investigated point-by-point by CCI. For each set of parameter values, experiments were performed at least in triplicate.

Results

Thereafter, we successively report the experimental data obtained with a single perforation, a spanwise row of perforations, and a staggered array of perforations. We only use propan-2-ol as a working liquid.

Single perforation

Fluid transfer in rim and curtain modes

For the reference case, i.e., $d = 4$ mm and $t = 1$ mm, we measure the fluid flow rate transferred through a single perforation. The supply flow rate on the front of the plate is swept up and down from 5 L h^{-1} to 38 L h^{-1} to investigate the rim mode, the inertial curtain mode, and the hysteretic curtain mode. Figure 3 presents the variations of the transferred volume flow rate per unit diameter of perforation (Q_t) as a function of the supply flow rate per unit width (Q). The same data are presented in a different way in Figure S2 (see Supplementary Material): we plot the variations of the overflow number (X) as a function of the supply Reynolds number (Re). We observe that the variations of Q_t (resp. X) in the rim mode are non-monotonous: Q_t (resp. X) first increases steeply with Q (resp. Re) and then decreases as Q (resp. Re) tends to Q_{cr} (resp. Re_{cr}). Q_t decreases less markedly than X since the increase of supply flow rate partly offsets the drop in liquid transfer efficiency. X reaches its peak value ($X = 0.67$) for $\mathrm{Re} = 25$. At Q_{cr} (resp. Re_{cr}), the transition from the rim to the (inertial) curtain mode occurs. As Q (resp. Re) is further increased beyond Q_{cr} (resp. Re_{cr}), Q_t (resp. X) grows. Ultimately, X seems to reach the plateau $X = 0.5$ corresponding to an equal partition of Q between the front and the back of the

perforation. As Q (resp. Re) is swept down from Q_{cr} (resp. Re_{cr}), the film flow remains in the curtain mode, and Q_t (resp. X) regularly reduces with the decrease in Q (resp. Re). We note that a minimal supply flow rate (resp. supply Reynolds number) is required for the liquid to be transferred through a perforation. In the rim mode, the threshold for liquid transfer is equal to $Q = 0.18$ m^3 m^{-1} h^{-1} (resp. Re $= 19$). In the hysteretic curtain mode, the liquid transfer stops when the curtain breaks, i.e. $Q = 0.10$ m^3 m^{-1} h^{-1} (resp. Re $= 11$).

When active, the rim mode is more efficient than the hysteretic curtain mode. However, the curtain modes (inertial and hysteretic) permit transfer over a broader range of supply flow rate. Furthermore, the variations of the transferred flow rate as a function of the supply flow rate are monotonous and more predictable when operating in curtain mode.

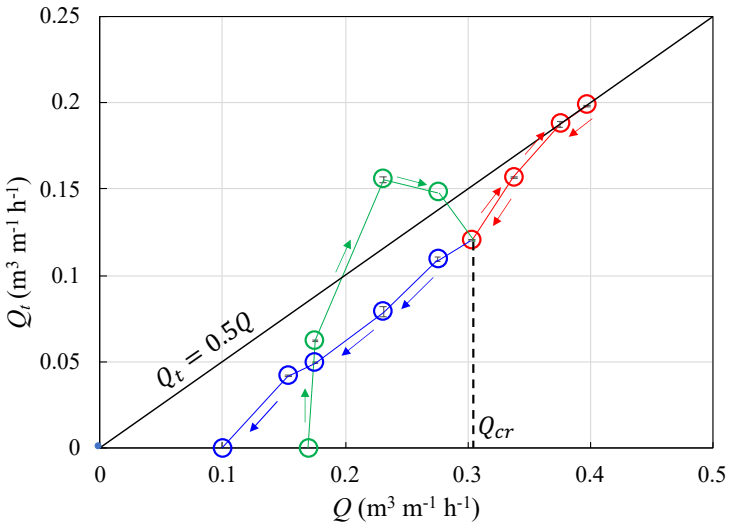

Figure 3. Transferred volume flow rate per unit diameter of perforation (Q_t) as a function of the supply flow rate (on the front of plate) per unit width (Q). Single isolated perforation. The diameter is $d = 4$ mm, the plate thickness $t = 1$ mm. The straight lines linking the dots are intended to guide the eye along the data points. Arrows indicate how Q_t evolves as Q is swept up and down. Rim mode (green), inertial curtain (red), hysteretic curtain (blue).

Effect of perforation diameter on liquid transfer in curtain mode

We focus on the curtain mode (either inertial or hysteretic) and measure the transferred volume flow rate as a function of the supply flow rate on the front of the plate, for six values of perforation diameter, i.e. $d = 4, 6, 8, 10, 14, 16$ mm. The plate thickness is $t = 1$ mm. Regardless of the value of d, the variations of Q_t with Q follow the same increasing trend (see Figure S3 in Supplementary Material and Figure 4). The liquid curtain ruptures and the liquid transfer ceases in the range $Q = 0.04$ to 0.1 $m^3\ m^{-1}\ h^{-1}$ (Re $= 5$ to 11). At lower Q values (larger than 0.1 $m^3\ m^{-1}\ h^{-1}$), the transferred flow rate Q_t is significantly lower (up to 30%) for $d = 4$ mm than for the other (larger) perforation diameters. The effect of d on Q_t decreases as Q increases. For the higher values of Q, the overflow number is close to $X = 0.5$ regardless of d.

Effect of plate thickness on fluid transfer in curtain mode

We measure the transferred volume flow rate in the curtain mode as a function of the supply flow rate for two plate thicknesses $t = 0.5$, 1 mm, and three perforation diameters $d = 4$, 6, 8 mm. There is a clear and significant effect of plate thickness on Q_t for $Q \gtrsim 0.3$ $m^3\ m^{-1}\ h^{-1}$ (Re $\gtrsim$ 30): all else being equal, the transfer is lower for smaller plate thickness $t = 0.5$ mm (see Figure 4). The overflow number at large Q values is close to 0.4 for $t = 0.5$ mm.

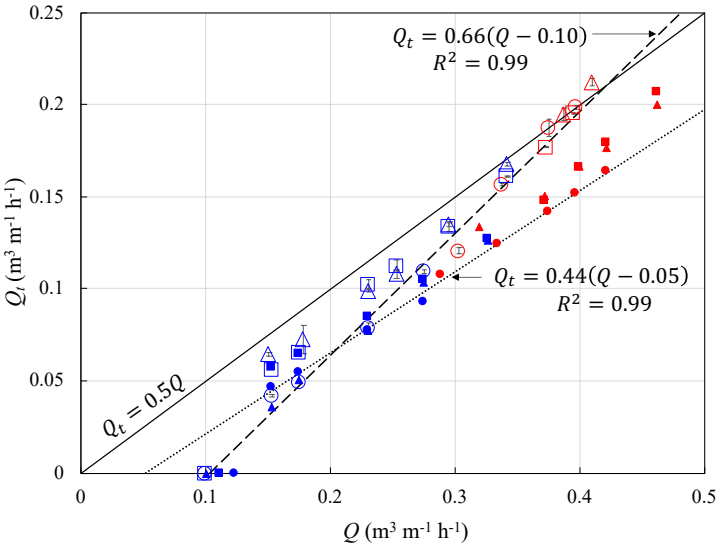

Figure 4. Transferred volume flow rate per unit diameter of perforation (Q_t) as a function of the supply flow rate (on the front of plate) per unit width (Q): effect of plate thickness. Single

perforation with $d = 4$ mm (circle), 6 mm (square), 8 mm (triangle), plate thickness $t = 0.5$ mm (filled), 1 mm (empty). Curtain mode (hysteretic in blue, inertial in red). Linear fit for $d = 4$ mm and $t = 0.5$ mm (dotted line), for $d = 4$ mm and $t = 1$ mm (dashed line).

Profile of the rivulet on the back of the plate

We focus on the curtain mode and examine how the transferred liquid spreads over the back of the plate for the reference case ($t = 1$ mm, $d = 4$ mm) and different values of the supply Reynolds number, i.e., Re = 24, 29, 33, 38, 42. We observe that the liquid leaks from the bottom edge of the perforation and forms a single rivulet. We measure its spanwise profile at $x = 2$, 20, 40, 60, 80, 100 mm from the bottom edge of the perforation (see Figure 5 and Figure S4 in Supplementary Material). We also measure its streamwise profile along $y = 0$ (see Figure S5 in Supplementary Material). Since the minimum measurable thickness of the CCI sensor is about 100 μm, we could not measure the thickness profile across the entire width of the rivulet and miss the thinner parts close to the contact line. Figures 5 and S4 show that the rivulet widens and flattens as it flows in the x-direction. The spanwise profile is approximately symmetric about the axis $y = 0$ and the thickness reaches its peak value close to $y = 0$. We observe slight deviations from symmetry: they are attributed to flow disturbances within the perforation and to wetting heterogeneities on the back of the plate. We exclude meandering instability since the volume flow rate out of the perforation is at least one order of magnitude lower than the meandering threshold[21]. Figure S5 shows that the rivulet is thicker as the supply Reynolds number increases. Streamwise profiles are slightly rough because the rivulet is not perfectly straight, the flow out of the perforation is not rigorously constant, and waves may travel on the rivulet surface.

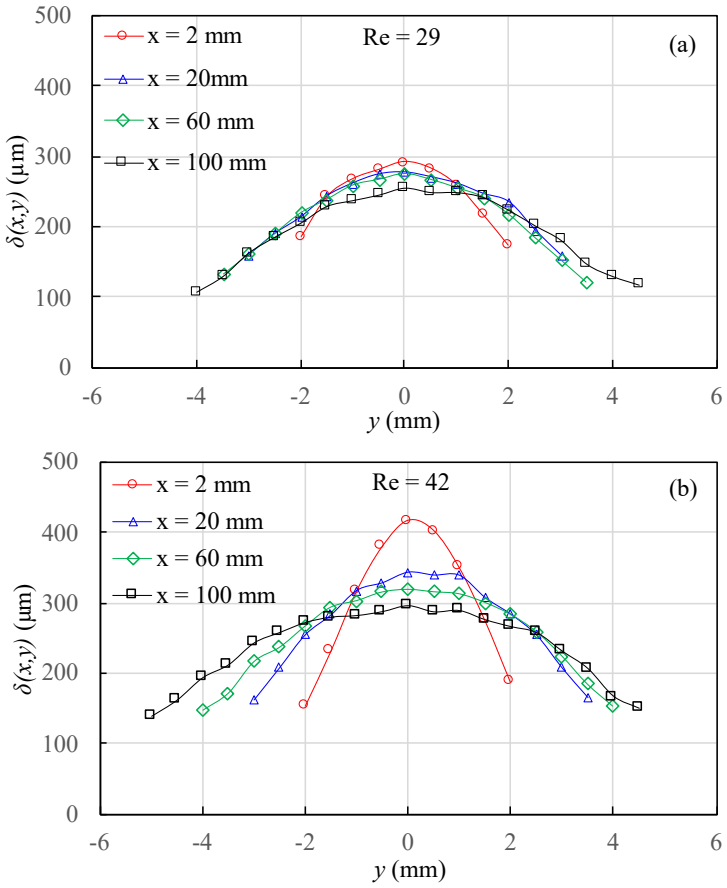

Figure 5. Spanwise rivulet profile at $x = 2$, 20, 60, 100 mm from the bottom edge of the perforation. Plate thickness $t = 1$ mm, perforation diameter $d = 4$ mm. Curtain mode. (a) Re $= 29$; (b) Re $= 42$. The lines linking the dots are intended to guide the eye along the data points.

Spanwise row of perforations

Effect of spacing on fluid transfer

We investigate the effect of one row of perforations on the liquid transfer from the front to the back of the plate. The perforation diameter is $d = 4$ mm and the plate thickness $t = 1$ mm. We study five perforation spacings $s = 6$, 8, 10, 12 and 14 mm. The supply flow rate on the front of the plate is swept up and down from 5 L h^{-1} to 38 L h^{-1} to investigate the rim mode, the inertial curtain mode, and the hysteretic curtain mode. The curtain Reynolds number, i.e., the Reynolds number at which curtain forms, ranges between 33 and 36 (see Figure S6 of the

Supplementary Material). These slight variations seem not correlated with the perforation spacing. Otherwise, Re_{cr} would increase with s: the broader the spacing, the more the flow can be deflected by a perforation, delaying the curtain transition. We instead believe that the variations in Re_{cr} are due to the variability of the plate curvature. A slight curvature of the sheet affects the liquid distribution upstream of the perforations and then the curtain transition. The residual curvature of the plate depends on its clamping within the frame.

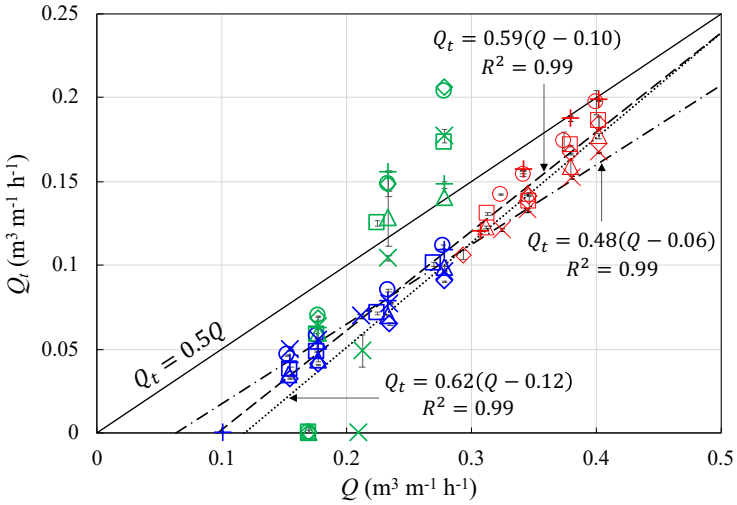

Figure 6. Average volume flow rate transferred per unit diameter of perforation (Q_t) as a function of the supply flow rate (on the front of plate) per unit width (Q): effect of perforation spacing (s). Perforation diameter $d = 4$ mm, perforation spacing $s = 6$ mm (×), 8 mm (◇), 10 mm (△), 12 mm (○), 14 mm (□), single isolated perforation or $s = \infty$ (+). Plate thickness $t = 1$ mm. Rim mode (green), inertial curtain mode (red), hysteretic curtain mode (blue). Linear fit on the curtain mode data for $s = 6$ mm (dashdotted line), $s = 8$ mm (dotted line), and $s = 14$ mm (dashed line).

In the rim mode, the onset of fluid transfer through the perforations occurs at $Q = 0.17$ $\mathrm{m^3\ m^{-1}\ h^{-1}}$ ($\mathrm{Re} = 19$) for all s except for $s = 6$ mm. In the latter case, the threshold is slightly greater: $Q = 0.21$ $\mathrm{m^3\ m^{-1}\ h^{-1}}$ ($\mathrm{Re} = 23$). As already observed for a single isolated perforation, at a given supply flow rate, the rim mode, when active, is more efficient than the curtain mode

to transfer fluid from the front to the back of the plate. Whatever the spacing, the variations of Q_t with Q in the rim mode follow the same increasing trend. However, at fixed Q, no rule emerges from the variations of Q_t with s. The highest transfer per perforation is obtained for $s = 8$ mm and $s = 12$ mm.

In the curtain mode (inertial and hysteretic), the dependence of Q_t on s is weaker. On average Q_t tends to be higher at greater perforation spacing.

Merging of the rivulets on the back of the plate

We focus on the curtain mode and examine how the rivulets, flowing from the perforations, merge downstream and tend to form a liquid film of even thickness. The plate thickness is fixed to $t = 1$ mm, the perforation diameter to $d = 4$ mm, five spacing are examined $s = 6$, 8, 10, 12, 14 mm and two Reynolds numbers $\mathrm{Re} = 26$ (hysteretic curtain mode) and $\mathrm{Re} = 38$ (inertial curtain mode).

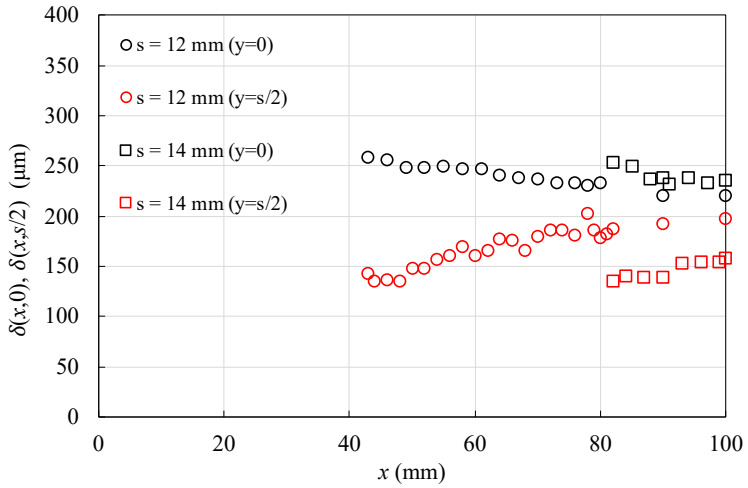

Figure 7. Streamwise film profile along $y = 0$ and $y = s/2$ for spacing $s = 12$, 14 mm. Single spanwise row of perforations, perforation diameter $d = 4$ mm, plate thickness $t = 1$ mm, and Reynolds number $\mathrm{Re} = 38$ (curtain mode).

We measure the streamwise film profile along $y = 0$ and $y = s/2$ (see Figure 7 and Figures S7 and S8 in Supplementary material). $y = 0$ (resp. $y = s/2$) coincides with a crest (resp. a trough)

of the free surface (see Figure 8). Since the minimum measurable thickness of the CCI sensor is about 100 µm, we cannot capture the beginning of the merging between two adjacent rivulets. Thus, at given spacing, merging starts at a distance slightly lower than the abscissa of the first measuring point along the line $y = s/2$ (Figures 7, S7, and S8). We observe that the film thickness along $y = 0$ (resp. $y = s/2$) decreases (resp. increases) with x and reaches a plateau. The smaller the spacing, the faster the plateau is reached and the higher is the plateau value. For the smaller spacing values, we note that the film thickness tends to decline after the plateau: this is due to the further spreading of the liquid film. We remind that the width of a perforation row (about 70 mm) is narrower than the channel width available for the liquid ($w = 90$ mm).

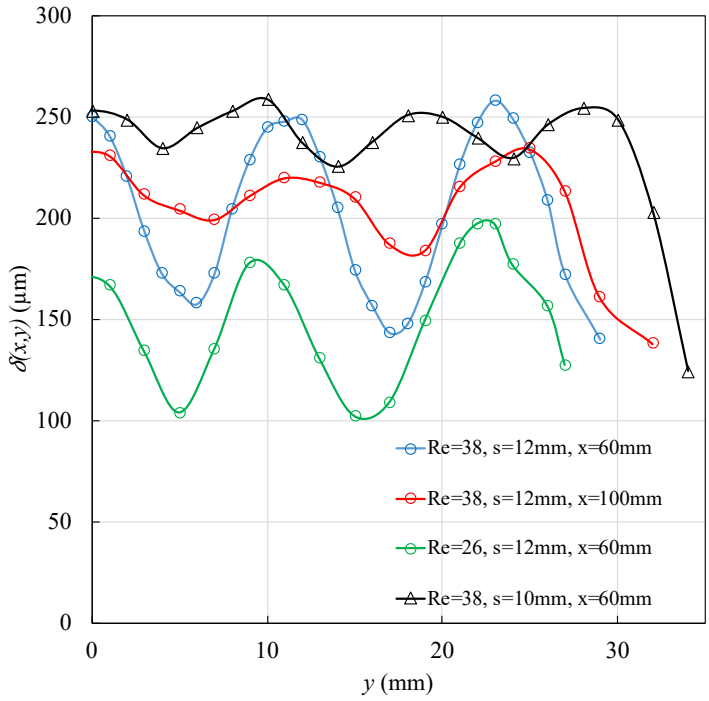

Figure 8. Film spanwise profiles for different streamwise locations (x), supply Reynolds numbers (Re) and perforation spacings (s). Single spanwise row of perforations, diameter $d = 4$ mm, plate thickness $t = 1$ mm, curtain mode. The lines linking the dots are intended to guide the eye along the data points.

Figure 8 shows spanwise film profiles at distances $x = 60$ mm and 100 mm. Rivulets have already merged. We observe that the profiles are still wavy with a wavelength close to the perforation spacing. The amplitude of these ripples decreases along with the x-axis (see the blue and the red curves in Figure 8): the film surface progressively levels as it flows downstream. At a given value of x and Re, the spanwise profile flattens faster with x and the average film thickness is larger when the perforation spacing is smaller (see the blue and the black curves in Figure 8). These findings are coherent with the observations of Figure 7. Last, all other things being equal, the average film thickness increases with the supply flow rate per unit width (see the blue and the green curves in Figure 8).

Staggered array of perforations

We perform experiments on a plate with a staggered array of perforations (up to 10 rows). The plate thickness is $t = 1$ mm, the perforation diameter $d = 4$ mm, and the spacing $s = 14$ mm. Perforations are spread laterally within 70 mm: odd (resp. even) rows comprise five perforations (resp. four). The opening rate of the perforation arrangement is equal to 6.4% (about half of the standard opening rate in industrial packing, that is 12.6%).

Observations

We sweep the supply flow rate on the front of the plate from $\mathrm{Re} = 10$ to Re_{cr} and beyond.

We distinguish three flow patterns depending on the supply Reynolds number.

At low Re ($\mathrm{Re} < 23$), the liquid film passes around the perforations of the odd numbered rows and flows in the curtain mode over the perforations of the even numbered rows. On the front of the plate, the perforations of the odd (resp. even) rows are topped by a U-shaped (resp. W-shaped) capillary ridge. There is no fluid transfer through the perforations of the odd rows: the contact line is pinned either at the top edge of the perforation or in its inner surface.

On the contrary, the fluid transfer is active in the perforations of the even rows. As the perforations of the odd rows deflect the liquid film, the spanwise distribution of flow rate per

unit width becomes strongly heterogeneous. The flow rate is depleted along $y = 0$ (modulo s) and enhanced along $y = s/2$ (modulo s), causing the film to flow in the curtain mode over the next (even numbered) row of perforations.

The alternation of row of perforations operating either in rim mode or in curtain mode is a consequence of the array symmetry and orientation with respect to the vertical. In industrial corrugated sheet packings, we expect perforations operating in curtain mode to coexist with perforation in rim mode, but their spatial distribution within the packing will not be as regular.

At $\mathrm{Re} = 23$, a liquid rim forms within the perforations of the odd rows. Then, at a moderate flow rate ($23 < \mathrm{Re} < \mathrm{Re}_{cr}$), the perforations of the odd rows operate in the rim mode, and those of the even rows are in the curtain mode (see Figure 9). On the back of the plate, all the perforations are topped by a U-shaped capillary ridge. A dry patch remains just below the perforations of the odd rows. Its area decreases as Re increases, and the patch finally disappears at even higher Re.

For the perforations operating in the rim mode, the liquid climbs over the top edge of the perforation (back of the plate), makes an arch-shaped capillary ridge and drains in the form of two parallel rivulets. Furthermore, the Kapitza waves traveling on the front of the plate make the rims oscillate. For the perforations in the curtain mode, the liquid leaks from the bottom edge of the perforation as a single rivulet. These observations are consistent with those for a single isolated perforation (see Problem description).

At $\mathrm{Re} = \mathrm{Re}_{cr}$, curtain transition is observed simultaneously for all odd rows. At Re_{cr} and above, all the perforations (odd and even numbered rows) operate in the curtain mode (see Figures S9 and S10 in Supplementary Material). The liquid leaks from the bottom edge of the perforations. The corresponding rivulets widen as they flow in the x-direction. The liquid free surface is disturbed by waves traveling downstream. This phenomenon is clearly seen beneath the third row of perforations (see Figure S10).

As the supply flow rate is swept down below $\mathrm{Re} = \mathrm{Re}_{cr}$, curtain mode and associated liquid transfer maintain in both odd and even rows. Curtain rupture is observed at low flow rates (about $\mathrm{Re} = 10$).

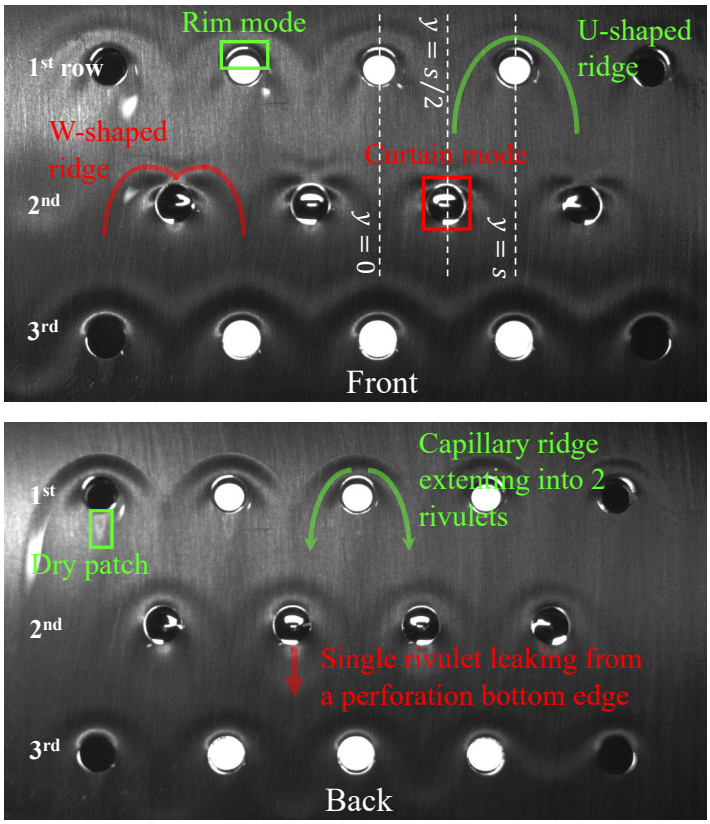

Figure 9. Liquid film pattern on a staggered array of perforations at Re = 23 when rim mode (in odd rows) and curtain mode (in even rows) coexist. Plate thickness $t = 1$ mm, perforation diameter $d = 4$ mm and spacing $s = 14$ mm. (Top) front of the plate, (bottom) back of the plate.

Fluid transfer

We measure the total volume flow rate on the back of the plate beneath the 1st, 2nd, 3rd and 10th row of perforations. We use plates with either 1, 2, 3, or 10 rows of perforations and collect the fluid on the back of the sheet using the dedicated collector (see Experimental set-up). We focus on the curtain mode, either hysteretic or inertial. We define the volume flow rate per unit width ($Q_b(k)$) flowing on the back of the plate downstream of the k^{th} row of perforations as the ratio

of the volume flow rate (m^3 h^{-1}) beneath the k^{th} row to the array width ($w_a = 70$ mm). Figure 10 presents the variations of Q_b as a function of the supply flow rate per unit width Q. We find that after ten rows of perforations, Q_b is already close to $Q/2$, the expected asymptotic limit (when the flows on the front and on the back of the plate equalize, and the liquid transfer vanishes). Beneath the third row of perforations, $Q_b(3)$ already reaches 65% to 90% of the final Q_b measured beneath the 10th row.

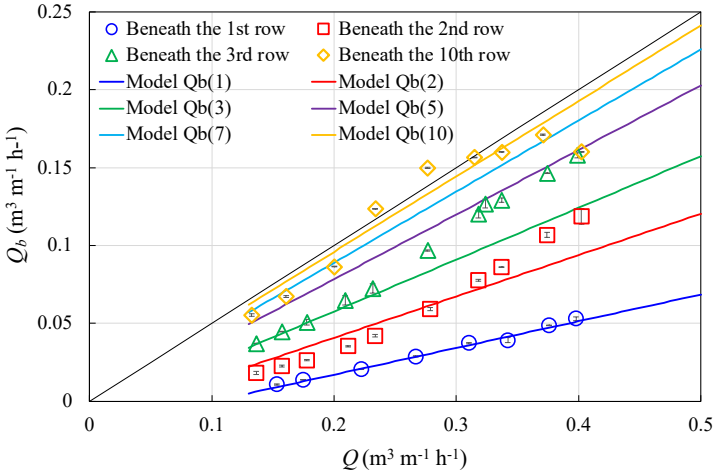

Figure 10. Volume flow rate per unit width (Q_b) on the back of the plate beneath the 1st, 2nd, 3rd and 10th row as a function of the supply flow rate per unit width on the front (Q). Plate thickness $t = 1$ mm, perforation diameter $d = 4$ mm, and spacing $s = 14$ mm. Curtain mode. The solid black line represents the asymptotic value of Q_b, i.e., after a large number of perforation rows. The beam of colored straight lines corresponds to the model predictions of Q_b flowing on the back of the plate after $k = 1$ to $k = 10$ rows of perforations.

Discussion

Hysteresis loop and liquid transfer thresholds

The variations of the transferred flow rate as a function of the supply flow rate (on the front of the plate) exhibit a hysteresis loop with two liquid transfer thresholds. The first one appears when the supply flow rate is increased from low values, the second when the flow rate is

decreased from values above the curtain transition (see Figures 3 and 6). In the former case, there is initially no fluid transfer from the front to the back of the plate: the contact line is pinned at the top edge of the perforation (front of the plate) or within its inner surface. As the contact line is released, the liquid transfer starts in the rim mode. This threshold is equal to $\mathrm{Re} = 19$ for $d = 4$ mm, $s \geq 8$ mm and $t = 1$ mm. In the latter case (flow rate descent), the liquid is transferred in hysteretic curtain mode, and the liquid transfer stops when the curtain breaks. This threshold is equal to about $\mathrm{Re} \cong 10$.

A similar hysteresis loop is reported by Gorodilov et al.[1]: they performed experiments on a structured packing perforated with slits and found that the liquid (water) transfer through the slits starts at $\mathrm{Re} \cong 1300$. They attributed this threshold to the liquid meniscus blockage at the slit entrance. Pavlenko et al.[1] found that for liquid nitrogen flowing on an aluminum sheet of 500.Y type packing, the liquid transfer through the perforations starts when $\mathrm{Re} \geq 100 - 160$. To reconcile our results with the literature data, we calculate the Weber number $\mathrm{We} = \rho Q^2/(\delta_{Nu}(Q)\sigma)$ which compares the inertia force (which triggers depinning) to the capillary force. We obtain $\mathrm{We} \cong 5$ from Gorodilov et al. data, $\mathrm{We} = 0.3 - 0.7$ from Pavlenko et al. and $\mathrm{We} = 0.27$ in our experiments. The agreement with Pavlenko et al. results is satisfactory. We could not explain the high Weber value estimated from Gorodilov et al..

Transferred volume flow rate per perforation (int the curtain mode)

The transferred volume flow rate through a single isolated perforation (in $\mathrm{m^3\ m^{-1}\ h^{-1}}$) reads $q_t = Q_t d$. Beneath a single row of perforations, the volume flow rate per unit width flowing on the back of the plate is given by $Q_b = Q_t d/s$. In the curtain mode, for $0.15 \leq Q \leq 0.5$ $\mathrm{m^3\ m^{-1}\ h^{-1}}$, Q_t is adequately described by a linear model $Q_t = p(Q - Q_{th})$ (see Figure S3, Figure 4, and Figure 6). The slope (p) and the threshold flow rate (Q_{th}) are obtained by least squares regression. Q_{th} lies in the Q range where curtain ruptures. p and Q_{th} depend on the plate thickness, on the perforation diameter, and on the perforation spacing. However, Figure S3 and

Figure 6 show that p and Q_{th} depend slightly on d and s in the range 4 mm $\leq d \leq$ 8 mm and 8 mm $\leq s \leq$ 14 mm, respectively. The dependence of p and Q_{th} on the plate thickness is more significant (see Figure 4). The effect of plate thickness can be explained by one of the mechanisms responsible for the so-called teapot effect[22]. At the top edge of a perforation on the front of the sheet (corresponding to the lip of the plate in Kistler & Scriven's analysis[38]), the liquid flow is deflected from the vertical direction toward the horizontal direction (parallel to the inner surface of the perforation). Since the liquid wets the inner surface of the perforation, this deflection increases with the plate thickness. Liquid transfer from the front to the back of the plate is expected to grow as well. The teapot effect[22] is driven by inertia, which may explain why the effect of plate thickness is more significant at higher values of the Reynolds number (see Figure 4). The teapot effect[22] also explains why the overflow number increases with Q (or with the supply Reynolds number Re) at fixed t.

For the standard perforation diameter $d = 4$ mm (used in industrial packing) and the plate thickness $t = 1$ mm, we retain that $Q_t[\mathrm{m^3\ m^{-1}\ h^{-1}}] = 0.66(Q - 0.10)$ for a single isolated perforation, $Q_t = 0.48(Q - 0.06)$ for s = 6 mm, and $Q_t = 0.60(Q - 0.10)$ for 8 mm $\leq s \leq$ 14 mm (linear fit on the curtain mode data for $s = 8$, 10, 12 and 14 mm, $R^2 = 0.98$, not displayed in Figure 10).

Rivulet spreading

We focus on a single isolated perforation with $d = 4$ mm and $t = 1$ mm. In the curtain mode, some liquid is systematically transferred through the perforation from the front to the back of the plate. The fluid leaks from the bottom edge of the perforation and forms a single rivulet on the back of the plate. The rivulet flattens and widens as it flows in the x-direction. Thereafter, we thoroughly analyze the rivulet spatial evolution and compare it to the model of Shetty & Cerro[16]. The derivation of the model and the checking of the assumptions in our experimental conditions are detailed in Appendix A8 of the Supplementary Material.

Following Shetty & Cerro[16], we fit the rivulet spanwise profiles with a Gaussian law:

$$\delta(x,y) = \delta_c(x)\exp\left(-\left(\frac{\left(y-y_c(x)\right)^2}{2\,m^2(x)}\right)\right) \quad (1)$$

$\delta_c(x)$ is the maximum film thickness, $y_c(x)$ the spanwise location of the peak, and $m(x)$ the standard deviation of the Gaussian, which measures the lateral spreading of the rivulet. We determine these parameters for each spanwise profile (at given supply Reynolds number Re and given x) using the least-squares method. The parameter values of the best fits are reported in Table 2 (in Appendix A8 of the Supplementary Material). The relative error is of the order of 1 to 2% for most of the fits, and it never exceeds 5%. We use $y_c(x)$ as a fitting parameter to improve the estimation of $\delta_c(x)$. However, since $y_c(x) \ll d$, we will neglect the deviation of the peak from $y = 0$ in the next analytical calculations and assume that the rivulet is symmetric about $y = 0$.

Figure 11 shows that the spanwise profiles collapse into a single curve when $\delta(x,y)$ and y are appropriately rescaled. We deduce that the rivulet spanwise profiles are self-similar and well described by a Gaussian law. These results concord with the findings of Shetty and Cerro[16]. We checked that the Gaussian law is a better approximation of the present rivulet profiles than the quartic similarity solution obtained by Duffy and Moffatt[27].

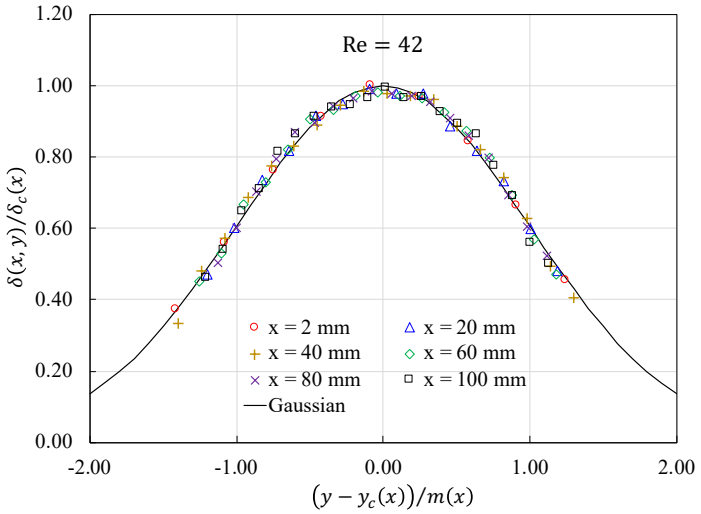

Figure 11. Collapse of the rivulet spanwise profiles with appropriate rescaling. Supply Reynolds number Re = 42 (inertial curtain mode). Data are well described by the Gaussian law (solid line).

If we further assume a Nusselt velocity profile within the rivulet thickness, the volume flow rate of the rivulet is given by

$$q_t = \frac{g}{3\nu}\sqrt{\frac{2\pi}{3}}\delta_c^3(x)\, m(x) \quad (2)$$

If this model is appropriate, the right-hand side of Eq. 2 calculated from the fitted Gaussian profile at the current abscissa x should be independent on x. We find that this quantity remains constant within a few percent along x for $x \geq x_0$ (see Figure S11 in Supplementary Material). $x_0 = 20$ mm for Re = 24, 29, 33 and $x_0 = 2$ mm for Re = 38, 42.

We expect that the rivulet thickness satisfies the thin-film equation[27]

$$\delta\frac{\partial^4\delta}{\partial y^4} + 3\frac{\partial\delta}{\partial y}\frac{\partial^3\delta}{\partial y^3} + 3\frac{\rho g}{\sigma}\frac{\partial\delta}{\partial x} = 0 \quad (3)$$

given for a steady rivulet flowing down a vertical plate.

If we restrict our analysis to $y = 0$, where the rivulet peaks, and assume a Gaussian spanwise profile centered at $y = 0$ (Eq. 1 with $y_c(x) = 0$), Eq. 3 becomes:

$$\frac{d\delta_c}{dx} + \frac{\sigma}{\rho g}\frac{\delta_c^2}{m^4} = 0 \quad (4)$$

We introduce the rescaled quantities:

$$x^{\#} = \frac{x - x_0}{2m(x_0)} \quad ; \quad \delta_c^{\#}(x) = \frac{\delta_c(x)}{\delta_c(x_0)} \quad ; \quad m^{\#}(x) = \frac{m(x)}{m(x_0)}$$

Using Eq. 1,2 and 4, we recover after a few calculations the scaling laws first established by Shetty & Cerro[16]:

$$\delta_c^{\#}(x^{\#}) = \left(1 + \frac{208}{3}\frac{\alpha^3}{\mathrm{Ca}}x^{\#}\right)^{-1/13} \quad (5)$$

$$m^{\#}(x) = \left(1 + \frac{208}{3}\frac{\alpha^3}{\mathrm{Ca}}x^{\#}\right)^{3/13} \qquad (6)$$

α and Ca are the aspect ratio and capillary number of the rivulet at $x = x_0$:

$$\alpha = \frac{\delta_c(x_0)}{2m(x_0)} \quad ; \quad \mathrm{Ca} = \frac{\mu}{\sigma}\left(\frac{g\delta_c^2(x_0)}{3\nu}\right)$$

The derivation of Eq. 5 and 6 involves the quantity $c_1 = 2\left(\delta_c^3(x)m(x)\right)^2$ (see Appendix A8 in the Supplementary Material). Since this quantity is not strictly conserved experimentally (even for $x > x_0$) and slightly fluctuates along x, it is relevant to distinguish between the "best" estimate of $2\left(\delta_c^3(x)m(x)\right)^2$ over the region $x > x_0$ (taken as its mean value) and denoted $\bar{c}_1$, and the value of $2\left(\delta_c^3(x)m(x)\right)^2$ at $x = x_0$, i.e., $c_0 = 2\left(\delta_c^3(x_0)m(x_0)\right)^2$. The former appears when removing m from Eq. 4 using Eq. 2. The latter appears when rescaling. Then, the argument of the power-laws (Eq. 5-6) should be transformed as follows:

$$\left(1 + \frac{208}{3}\frac{\alpha^3}{\mathrm{Ca}}x^{\#}\right) \rightarrow \left(1 + \frac{208}{3}\frac{\alpha^3}{\mathrm{Ca}}\beta x^{\#}\right) \qquad (7)$$

with $\beta = \left(\frac{c_0}{\bar{c}_1}\right)^2$. We recast the data of Table 2 (Supplementary Material) for $x > x_0$ into $\left(1 + \frac{208}{3}\frac{\alpha^3}{\mathrm{Ca}}\beta x^{\#}\right)$, $\delta_c^{\#}$, and $m^{\#}$. We plot them on log-log scale in Figure 12. We observe that the thickness (resp. width) data collapse into a single line with a slope equal to -0.075 (resp. 0.25), very close to the theoretical slope $-1/13 \cong -0.077$ (resp. $3/13 \cong 0.23$) originally established by Shetty & Cerro[16] and Duffy & Moffatt[27]. We retain that, far downstream of the perforation, the rivulet peak-thickness (resp. width) decreases as $x^{-0.075}$ (resp. $x^{0.25}$), very close to $x^{-1/13}$ (resp. $x^{3/13}$).

We remind that the theoretical exponents $1/13$ and $3/13$ characterize the rivulet spreading when driven by the capillary pressure (as opposed to hydrostatic pressure). This is indeed the case for the rivulet falling down a vertical plate.

These small exponents (in absolute value) explain why the rivulet pattern may persist over the whole height of a corrugated sheet packing[7].

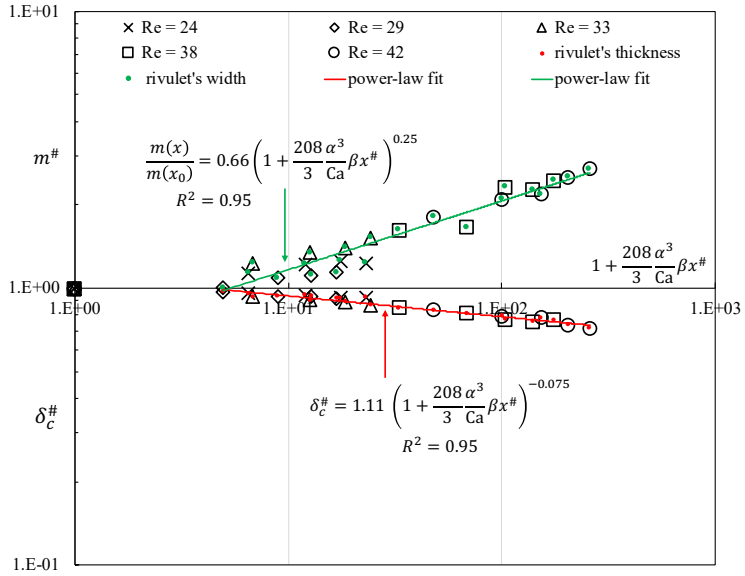

Figure 12. Rescaled peak film thickness and width as a function of the rescaled streamwise coordinate. Data (except the point (1;1)) are fitted with a power-law using the least-squares method.

Rivulet merging and film leveling

Figures 7, S7, and S8 show the merging dynamics of adjacent rivulets for $d = 4$ mm, $t = 1$ mm, Re $= 38$ and $s = 6$, 8, 10, 12, 14 mm. We roughly consider that the onset of merging happens close to the first measuring point (point with the smallest x-value at fixed s) on the centerline between two perforations ($y = s/2$). Then, we deduce that as the perforation spacing increases, the merging of the rivulets occurs further downstream. When the spacing increases from 10 mm to 12 mm, i.e., by 20%, the distance between the onset of merging and the row of perforations doubles.

The results established for a single rivulet help explain the strong effect of s on the rivulet merging. If the rivulet half-width at a distance x from the perforation is approximately equal to

$2m(x)$, two adjacent rivulets start to merge when $4m(x) \approx s$. We deduce that the rescaled distance $x_{mer}^{\#}$ between the onset of merging and the row of perforations satisfies:

$$1 + \frac{208}{3}\frac{\alpha^3}{\mathrm{Ca}} x_{mer}^{\#} \cong \left(\frac{s}{4m(x_0)}\right)^{13/3} \qquad (8)$$

The prominent exponent (13/3) explains the strong effect of s on the onset of merging. As seen earlier, it is relevant to introduce the correction factor β:

$$1 + \frac{208}{3}\frac{\alpha^3}{\mathrm{Ca}} \beta x_{mer}^{\#} \cong \left(\frac{s}{4m(x_0)}\right)^{13/3} \qquad (9)$$

The left-hand side of Eq. 9 is estimated for $\mathrm{Re} = 38$ and $s = 6, 8, 10, 12, 14$ mm from the data of Figures 7, S7, and S8. Figure S12 (Supplementary material) presents the variations of $1 + \frac{208}{3}\frac{\alpha^3}{\mathrm{Ca}} \beta x_{mer}^{\#}$ as a function of $s/\left(4m(x_0)\right)$. The data points are fitted by a power law using the least-squares method. The exponent (4.58) is close to the theoretical value ($13/3 = 4.33$). The prefactor (4.73) is significantly greater than the expected value (1). We presently overestimate $x_{mer}^{\#}$ because the first measuring point (corresponding to a film thickness close to 100 μm) used to estimate the onset of merging is systematically located downstream of the actual position where the rivulets start to merge (corresponding to a vanishing film thickness).

Let us now examine how the surface of the film formed from the recently merged rivulets relaxes downstream to a flat free surface. As seen earlier, the local film thickness $\delta(x, y)$ satisfies the thin-film equation, i.e., Eq. 3. Figure 8 suggests describing the film surface as a sine wave. We thus seek a solution of the form:

$$\delta(x, y) = \delta_\infty \left(1 + \varepsilon(x) \cos\left(\frac{2\pi y}{s}\right)\right) \qquad (10)$$

where δ_∞ is the flat-film thickness (reached far downstream of the perforation row) and ε the dimensionless perturbation amplitude of the film thickness. We consider $\varepsilon(x) \ll 1$.

We replace Eq. (10) into Eq. (3). Calculation under first-order approximation leads to:

$$\varepsilon(x) = \frac{\delta(x_{mer}, 0) - \delta_\infty}{\delta_\infty} \exp\left(-\left(\frac{x - x_{mer}}{\mathcal{L}}\right)\right) \quad (11)$$

x_{mer} corresponds to the streamwise location where the rivulets start to merge. The film surface relaxes exponentially with streamwise coordinate. The characteristic length of the relaxation to a flat surface is given by

$$\mathcal{L} = \frac{3s^4}{(2\pi)^4 l_c^2 \delta_\infty} \quad (12)$$

where $l_c = \sqrt{\sigma/\rho g}$ is the capillary length. Let us recast the data of Figures 7, S7, and S8 into $(x - x_{mer})/\mathcal{L}$ and $\big(\delta(x,0) - \delta(x,s/2)\big)/\big(\delta(x_{mer},0) - \delta(x_{mer},s/2)\big)$, and plot them in Figure 13. The flat-film thickness (δ_∞) is presently estimated as the mean value of $\big(\delta(x,0) + \delta(x,s/2)\big)/2$ over x. We calculate that $\mathcal{L}$ ranges from 3.3 mm for $s = 6$ mm to 121 mm for $s = 14$ mm. We observe that all the data collapse into a single exponential curve. The characteristic length of the exponential decay is equal to $\mathcal{L}/1.36$, in good agreement with the theoretical prediction.

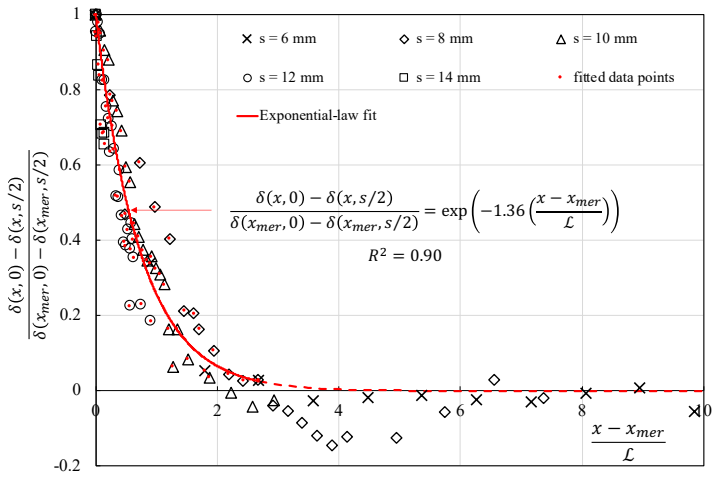

Figure 13. Rescaled perturbation amplitude of the liquid film flowing on the back of the plate as a function of the rescaled streamwise coordinate. Single row of perforations, perforation diameter $d = 4$ mm, plate thickness $t = 1$ mm, and Reynolds number Re $= 38$ (curtain

mode). The data points with red dots are fitted with an exponential law using the least-squares method (red solid line extended with dashes).

We note that the flat-film thickness (δ_∞) depends on the volume flow rate per unit width flowing on the back of the plate (Q_b) via $\delta_{Nu}(Q_b) = (3\nu Q_b/g)^{1/3}$. Since $Q_b = Q_t\, d/s$, we deduce from Eq. 12 that at given supply flow rate on the front of the plate, the characteristic length of the film relaxation (on the back of the plate) scales as $s^{13/3}$.

Flow balancing between the front and the back of the plate

Let us analyze the variations of the volume flow rate per unit width on the back of the plate, along with a staggered array of perforations. We propose a simple recurrence model that gives the volume flow rate per unit width on the back of the plate just downstream the kth row of perforations ($Q_b(k)$) as a function of the flow rates per unit width just downstream of the (k-1)th row of perforations, i.e., $Q(k-1)$ on the front of the plate and $Q_b(k-1)$ on the back. The variations of $Q(k-1)$ and $Q_b(k-1)$ over the array width are not taken into account. $Q(k-1)$ and $Q_b(k-1)$ represent volume flow rates per unit width averaged over the width. We suppose that all the perforations of the plate operate in the curtain mode.

For $d = 4$ mm, $t = 1$ mm, and $s = 14$ mm, we found (first paragraph of the discussion) that the transferred volume flow rate per unit diameter of perforation through the first row of perforations is well described by

$$Q_t(k=1)[\mathrm{m^3\ m^{-1}\ h^{-1}}] = 0.6(Q(0) - 0.1)$$

where $Q(0) = Q$ is the supply flow rate per unit width on the front of the plate.

To establish an analogous relationship for the next rows ($k > 1$), we first estimate the curtain flow over a perforation as $d_p\big(Q(k-1) + Q_b(k-1)\big)$ and consider that this flow divides equally between the front and the back of the plate. Then, the transferred volume flow rate per unit diameter of perforation through the kth row of perforations expresses as

$$Q_t(k) = \big(Q(k-1) - Q_b(k-1)\big)/2$$

$Q_t(k)$ is counted positively from the front to the back. The volume flow rate per unit width on the back of the plate beneath the kth row of perforations is given by:

$$Q_b(k) = Q_b(k-1) + \frac{d}{s} Q_t(k)$$

And the volume flow rate per unit width on the front of the plate beneath the kth row of perforations:

$$Q(k) = Q(k-1) - \frac{d}{s} Q_t(k)$$

In this formulation, we implicitly suppose that the number of perforations per row is large ($N - 1 \cong N$) and we neglect what happens on the lateral borders of the array.

The model is computed for $k = 1$ to $k = 10$, and the results are reported in Figure 10 and Figure S13 (Supplementary Material). $Q_b(k)$ flowing on the back of the plate beneath the kth row of perforations varies linearly with the supply flow rate $Q(0)$ (see the colored straight lines of Figure 10). We observe that the model adequately describes the variations of the volume flow rate per unit width on the back of the plate when the supply volume flow rate $Q(0)$ is low. For high values of $Q(0)$, the model underestimates the liquid transfer. We advance that the flow inertia pushes the liquid curtain to the back of the plate (teapot effect[22]), which affects the partition of the curtain flow between the front and the back: the liquid transfer from the front to the back is then enhanced.

Figure S13 shows that the volume flow rates on the front and the back of the plate tend to equalize as the row number (k) increases. The transferred volume flow rate decreases with k since the driving force ($Q(k-1) - Q_b(k-1)$) decreases. Q_b reaches 90% of its asymptotic value ($Q(0)/2$) beneath the 7th row of perforations.

Conclusion

To better understand the effect of the perforations on the liquid redistribution in corrugated sheet packings, we considered a simplified but relevant configuration. We studied the liquid transfer from the front to the back of a vertical flat perforated sheet: we solely supplied the front of the plate with liquid (above the first perforation row), and we examined how the perforations irrigate the back of the plate. We essentially performed our experiments with all the perforations operating in the curtain mode. In that case, a liquid curtain closes each perforation. On the bottom edge of the perforations, the curtain flow divides between the plate's front and back. The transferred liquid leaks in the form of rivulets (one per perforation). We measured the transferred volume flow rate through the perforations and characterized the spreading and merging of the rivulets on the back of the plate. We successively investigated plates with a single perforation, a spanwise row of perforations, and a staggered array of perforations.

Single perforation and spanwise row of perforations: we found that the transferred volume flow rate per unit diameter of perforation (Q_t) varies linearly with the supply flow rate per unit width (Q). For the standard perforation diameter $d = 4$ mm, the plate thickness $t = 1$ mm, the perforation spacing (center-to-center) lying in the range 8 mm $\leq s \leq$ 14 mm, and the supply flow rate per unit width in the interval 0.15 $m^3\ m^{-1}\ h^{-1} < Q <$ 0.4 $m^3\ m^{-1}\ h^{-1}$, Q_t is well described by $Q_t[m^3\ m^{-1}\ h^{-1}] = 0.60(Q - 0.10)$.

The rivulet leaking from a perforation widens (resp. flattens) as the 0.25 (resp. -0.075) power of the traveled distance from the perforation (after appropriate rescaling). Adjacent rivulets merge into a continuous wavy film at a traveled distance which scales as the 4.58 power of the perforation spacing. The scaling exponents are very close to the theoretical exponents established by Shetty & Cerro[16] and Duffy & Moffatt[27] for a rivulet spreading in the capillary-dominant regime.

The wavy surface of the newly formed film relaxes downstream to a flat surface. The amplitude of crests and troughs at the film surface decay exponentially with the streamwise coordinate.

The characteristic length of this relaxation theoretically scales as the 13/3 power of the perforation spacing.

Staggered array of perforations: From one row of perforations to another, the volume flow rate per unit width (and averaged over the width) flowing on the back (resp. front) of the plate increases (decreases) and relaxes toward its asymptotic value. This value is equal to half the supply flow rate. Beneath the third row of perforations, the flow rate on the back of the plate already reaches 65% to 90% of its asymptotic value. The relaxation is more rapid as the supply flow rate increases: we expect that the teapot effect[22] (driven by the flow inertia) enhances the liquid transfer from the front to the back of the plate.

Finally, we propose a simple recurrence model that gives the volume flow rate per unit width on the back of the plate beneath each row of perforations. This model adequately represents the data obtained at low supply flow rate. It predicts that the flow rate on the back of the plate reaches 90% of its asymptotic value beneath the 7^{th} row of perforations.

The present work provides helpful insight into the elementary mechanisms involved in the liquid redistribution through perforations. In the future, we plan to extend this study to vertical perforated sheets with horizontal corrugations as a next step to understand the interplay between perforations and corrugations.

Acknowledgments

This research was supported by Air Liquide Research & Development and by Association Nationale de la Recherche et de la Technologie ANRT (CONVENTION CIFRE N° 2017/1472). The authors express their gratitude to Sebastien Gauthier and Frederic Lesage for their technical contribution to the project.

Bibliography

1. Gorodilov AA, Berengarten MG, Pushnov AS. Features of fluid film falling on the corrugated surface of structured packings with perforations. *Theor Found Chem Eng*. 2016;50(3):325-334.
2. Fourati M, Roig V, Raynal L. Experimental study of liquid spreading in structured packings. *Chem Eng Sci*. 2012;80:1-15.
3. Singh RK, Galvin JE, Sun X. Hydrodynamics of the rivulet flow over corrugated sheet used in structured packings. *Int J Greenh Gas Control*. 2017;64(February):87-98.
4. Singh RK, Galvin JE, Sun X. Three-dimensional simulation of rivulet and film flows over an inclined plate: Effects of solvent properties and contact angle. *Chem Eng Sci*. 2016;142:244-257.
5. Edwards DP, Krishnamurthy KR, Potthoff RW. Development of an improved method to quantify maldistribution and its effect on structured packing column performance. *Chem Eng Res Des*. 1999;77(7):656-662.
6. Janzen A, Steube J, Aferka S, et al. Investigation of liquid flow morphology inside a structured packing using X-ray tomography. *Chem Eng Sci*. Published online 2013.
7. Schug S, Arlt W. Imaging of Fluid Dynamics in a Structured Packing Using X-ray Computed Tomography. *Chem Eng Technol*. 2016;39(8):1561-1569.
8. Wehrli M, Kögl T, Linder T, Arlt W. An unobstructed view of liquid flow in structured packing. *Chem Eng Trans*. 2018;69(2016):775-780.
9. Yao Y, Pavlenko AN, Volodin OA. Effects of layers and holes on performance of wire mesh packing. *J Eng Thermophys*. 2015;24(3):222-236.
10. Pavlenko AN, Volodin OA, Surtaev AS. Hydrodynamics in falling liquid films on surfaces with complex geometry. *Appl Therm Eng*. 2017;114:1265-1274.
11. Pavlenko AN, Pecherkin NI, Zhukov VE, Meski G, Houghton P. Overview of methods to control the liquid distribution in distillation columns with structured packing: Improving separation efficiency. *Renew Sustain Energy Rev*. Published online 2020.
12. Xie H, Hu J, Wang C, Dai G. Liquid flow transition and confined free film formation on a vertical plate with an open window. *Exp Therm Fluid Sci*. 2018;92(July 2017):174-183.
13. Xie H, Hu J, Dai G. Numerical simulation on flow behavior of twin-liquid films over a vertical plate with an open window. *AIChE J*. 2018;64(4):1458-1468.

14. Iyer M, Duval H, Casalinho J, Seiwert J, Wattiau M. Experimental study of a liquid film flowing over a perforation. 2021;(March).
15. Hu J, Yang X, Yu J, Dai G. Carbon dioxide (CO2) absorption and interfacial mass transfer across vertically confined free liquid film-a numerical investigation. *Chem Eng Process Process Intensif*. 2017;111:46-56.
16. Shetty SA, Cerro RL. Spreading of Liquid Point Sources over Inclined Solid Surfaces. *Ind Eng Chem Res*. 1995;34(11):4078-4086.
17. Smith BPC. A similarity solution for slow viscous f l o w down an inclined plane. 1973;58:275-288.
18. Duffy BR, Moffatt HK. A similarity solution for viscous source flow on a vertical plane. *Eur J Appl Math*. 1997;8(1):37-47.
19. Wilson SK, Duffy BR, Davis SH. On a slender dry patch in a liquid film draining under gravity down an inclined plane. *Eur J Appl Math*. 2001;12(3):233-252.
20. Nusselt W. *Die Oberflächenkondensation Des Wasserdampfes*.; 1916.
21. Le Grand-Piteira N, Daerr A, Limat L. Meandering rivulets on a plane: A simple balance between inertia and capillarity. *Phys Rev Lett*. 2006;96(25).
22. Kistler SF, Scriven LE. The Teapot Effect: Sheet-Forming Flows With Deflection, Wetting and Hysteresis. *J Fluid Mech*. 1994;263:19-62.

Supplementary Material

A1. Rim mode and curtain mode: typical flow patterns

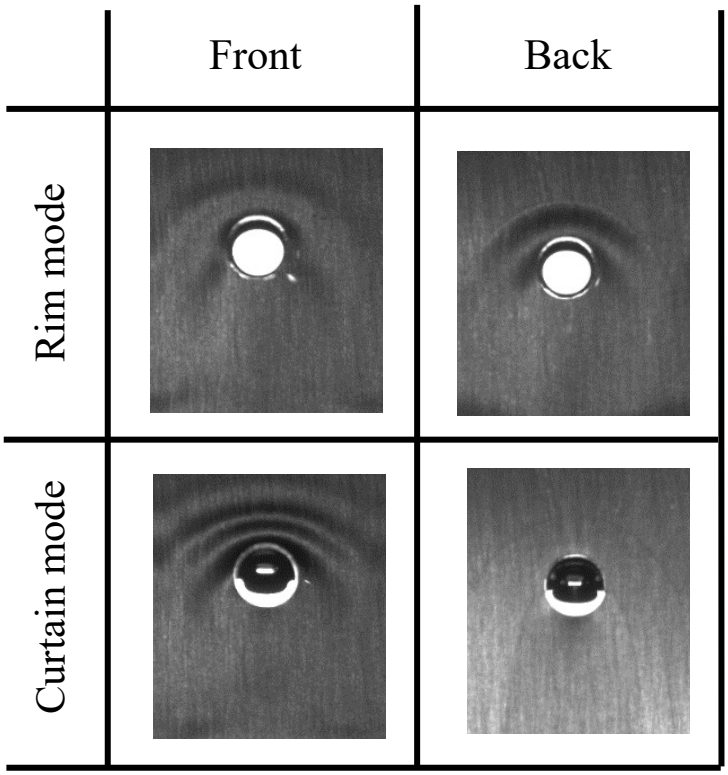

Figure S1. Flow patterns on the front and back of the plate in the rim mode and curtain mode.

The top of Figure S1 presents the typical flow pattern encountered in the rim mode: a liquid rim forms within the perforation and covers its inner surface. On the front of the plate, the perforation is topped by a capillary ridge. On the back, the liquid climbs over the top edge of the perforation and makes a capillary ridge that extends in the form of two parallel rivulets.

In the curtain regime (bottom of Figure S1), the liquid fills the perforation. On the front of the plate, the perforation is topped by a train of capillary ridges. On the back of the plate, the liquid leaks from the bottom edge of the perforation in the form of a single rivulet.

A2. Liquid properties

Liquid	ρ (kg m^{-3})	μ (mPa s)	σ (mN m^{-1})	θ (°)	Ka	Re range
Propan-2-ol	786[a]	2.05[b]	21[c]	11º-17º[a]	348	10 - 45

[a]measured, [b]from†, [c]from‡.

Table 1. Physical properties of propan-2-ol at 25°C and range of Reynolds number investigated. The bounds of the contact angle (θ) interval correspond to the receding contact angle and to the advancing contact angle, respectively. The equilibrium contact angle (θ_E) lies in-between.

Table 1 reports the physical properties of the working fluid, i.e. propan-2-ol. We stress that the wetting of the aluminum sheets with propan-2-ol is highly favorable: the contact angle lies between 11° and 17°. We introduce the Kapitza number of the liquid, it compares surface tension to the viscous and gravitational effects, i.e., $\mathrm{Ka} = \sigma/\left(\rho g^{1/3}\nu^{4/3}\right)$. Re is the film Reynolds number, defined in the Problem description (see the main document).

†Paez S, Contreras M. Densities and Viscosities of Binary Mixtures of 1-Propanol and 2 Propanol with Acetonitrile. J Chem Eng Data. 1989;34(4):455-459. doi:10.1021/je00058a025

‡Vazquez G, Alvarez E, Navaza JM. Surface Tension of Alcohol + Water from 20 to 50 °C. J Chem Eng Data. 1995;40(3):611-614. doi:10.1021/je00019a016

A3. Liquid transfer from a single perforation

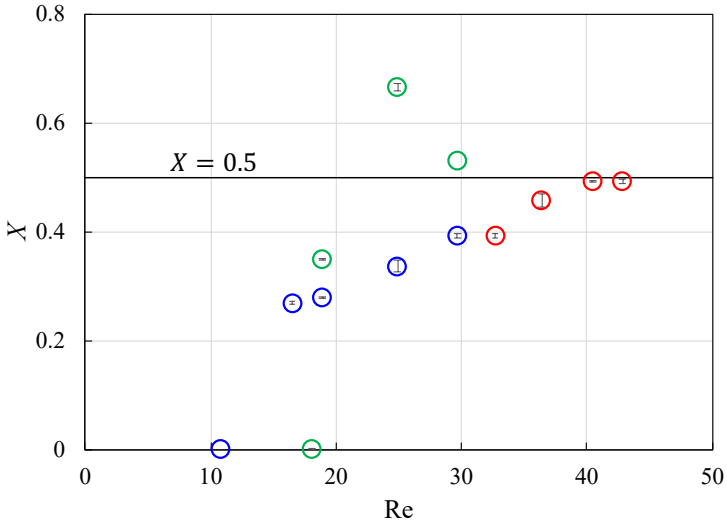

Figure S2. Overflow number (X) as a function of the supply Reynolds number (Re). Single isolated perforation. The diameter is $d = 4$ mm, the plate thickness $t = 1$mm. Rim mode (green), inertial curtain (red), hysteretic curtain (blue).

Following Gorodilov et al.[1] , we plot (Figure S2) the variations of the overflow number (X) as a function of the supply Reynolds number (Re). We observe that the variations of X in the rim mode are non-monotonous: X first increases steeply with Re and then decreases as Re tends to Re_{cr}. X reaches its peak value ($X = 0.67$) for $\mathrm{Re} = 25$. At Re_{cr}, the transition from the rim to the (inertial) curtain mode occurs. As Re is further increased beyond Re_{cr}, X grows. Ultimately, X seems to reach a plateau $X = 0.5$ corresponding to an equal partition of Q between the front and the back of the perforation. As Re is swept down from Re_{cr}, the film flow remains in the curtain mode, and X regularly reduces with the decrease in Re.

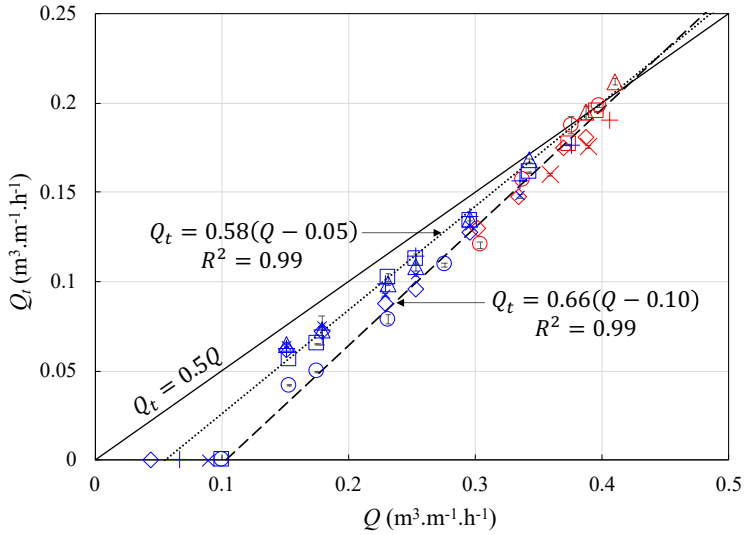

Figure S3. Transferred volume flow rate per unit diameter of perforation (Q_t) as a function of the supply flow rate (on the front of plate) per unit width (Q): effect of the perforation diameter. Single perforation with $d = 4$ mm (○), 6 mm (□), 8 mm (△), 10 mm (◇), 14 mm (×), 16 mm (+), plate thickness $t = 1$ mm. Curtain mode (hysteretic in blue, inertial in red). Linear fit for $d = 4$ mm (broken line), for $d = 8$ mm (dotted line).

We focus on the curtain mode (either inertial or hysteretic) and measure the transferred volume flow rate as a function of the supply flow rate on the front of the plate, for six values of perforation diameter, i.e., $d = 4$, 6, 8, 10, 14, 16 mm. The plate thickness is $t = 1$ mm. Regardless of the value of d, the variations of Q_t with Q follow the same increasing trend (Figure S3). The liquid curtain ruptures and the liquid transfer ceases in the range $Q = 0.04$ to 0.1 m^3 m^{-1} h^{-1} (Re $= 5$ to 11). At lower Q values (larger than 0.1 m^3 m^{-1} h^{-1}), the transferred flow rate Q_t is significantly lower (up to 30%) for $d = 4$ mm than for the other (larger) perforation diameters. The effect of d on Q_t decreases as Q increases. For the higher values of Q, the overflow number is close to $X = 0.5$ regardless of d.

A4. Rivulet from a single perforation: spanwise and streamwise profiles

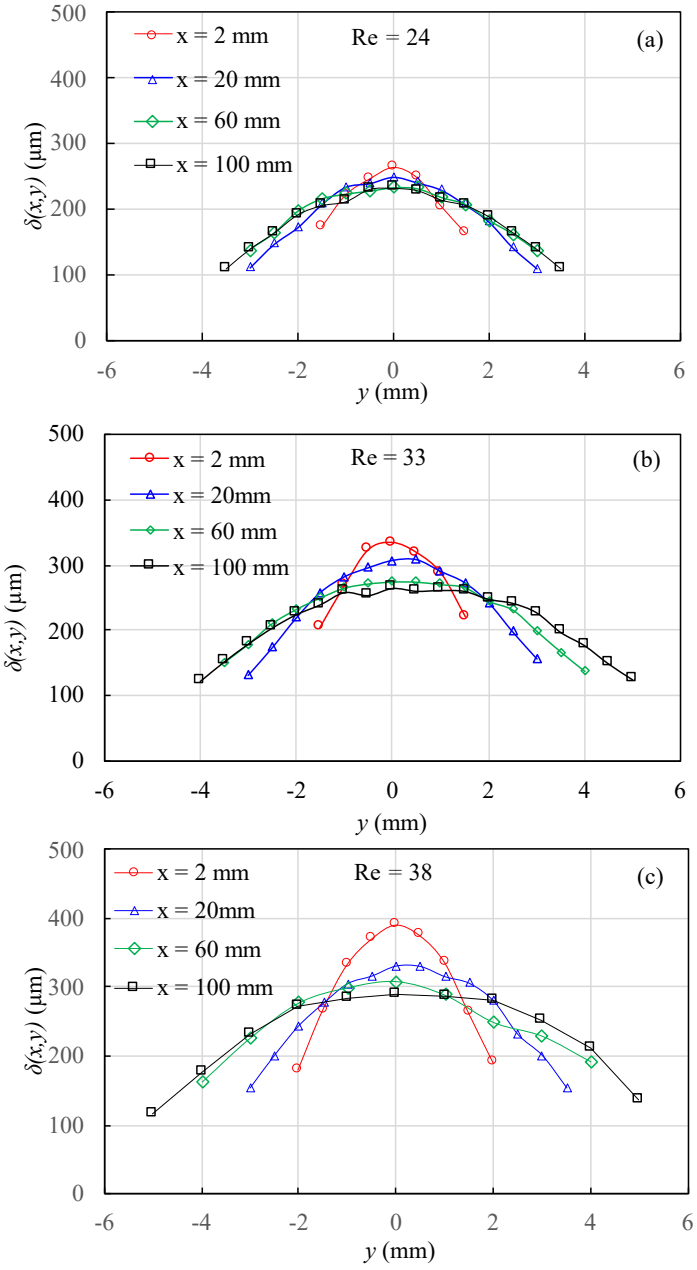

Figure S4. Spanwise rivulet profile at $x = 2$, 20, 60, 100 mm from the bottom edge of the perforation. Plate thickness $t = 1$ mm, perforation diameter $d = 4$ mm. Curtain mode. (a) $\mathrm{Re} = 24$; (b) $\mathrm{Re} = 33 = \mathrm{Re}_{cr}$; (c) $\mathrm{Re} = 38$. The lines linking the dots are intended to guide the eye along the data points.

Figure S4 completes the Figure 5 displayed in the main document and presents the rivulet spanwise profiles for supply Reynolds number Re = 24, 33, 38. We observe that the rivulet

widens and flattens as it flows in the x-direction. The spanwise profile is approximately symmetric about the axis $y = 0$ and the thickness reaches its peak value close to the line $y = 0$. Figure S5 presents the streamwise rivulet profile along the line $y = 0$ for different values of the supply Reynolds number. The rivulet flattens as it flows down the plate. At given streamwise position, the rivulet thickness increases with the supply Reynolds number. Streamwise profiles are slightly rough because the rivulet is not perfectly straight, the flow out of the perforation is not rigorously constant, and waves may travel on the rivulet surface.

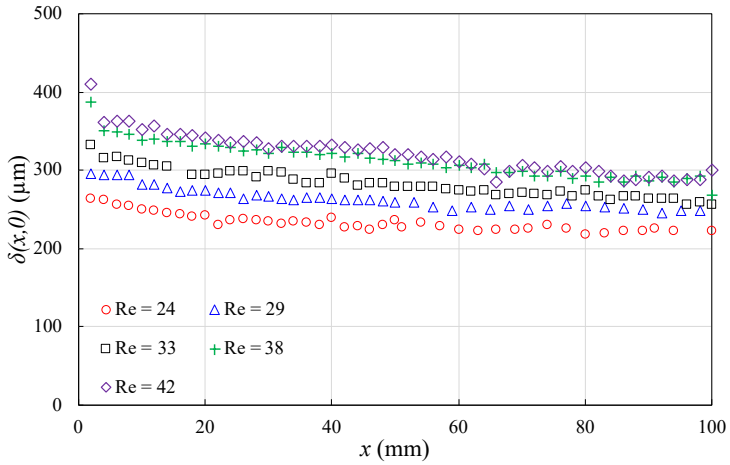

Figure S5. Streamwise rivulet profile along $y = 0$ for different values of the supply Reynolds number, Re $= 24, 29, 34, 38, 42$. Plate thickness $t = 1$ mm, perforation diameter $d = 4$ mm. Curtain mode.

A5. Effect of the perforation spacing on the curtain Reynolds number

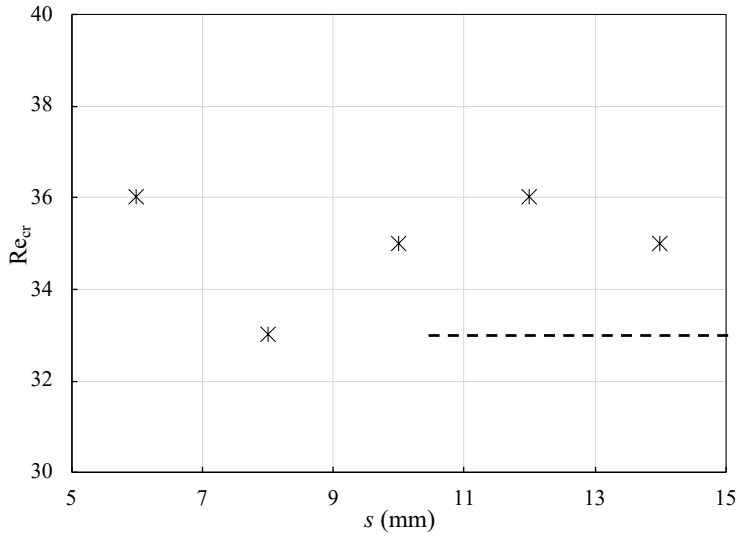

Figure S6. Curtain Reynolds number determined for different values of the perforation spacing, $s = 6$, 8, 10, 12, 14 mm. Perforation diameter $d = 4$ mm and plate thickness $t = 1$ mm. The broken line corresponds to the curtain Reynolds number for a single isolated perforation ($s = \infty$).

Figure S6 summarizes the curtain Reynolds number (Re_{cr}) values determined for different perforation spacings. It appears that Re_{cr} ranges between 33 and 36. These slight variations seem not correlated with the perforation spacing. Otherwise, Re_{cr} would increase with s: the broader the spacing, the more the flow can be deflected by a perforation, delaying the curtain transition. We instead believe that the variations in Re_{cr} are due to the variability of the plate curvature. A slight curvature of the sheet affects the liquid distribution upstream of the perforations and then the curtain transition. The residual curvature of the plate depends on its clamping within the frame.

A6. Merging of the rivulets flowing from a row of perforations: streamwise profiles

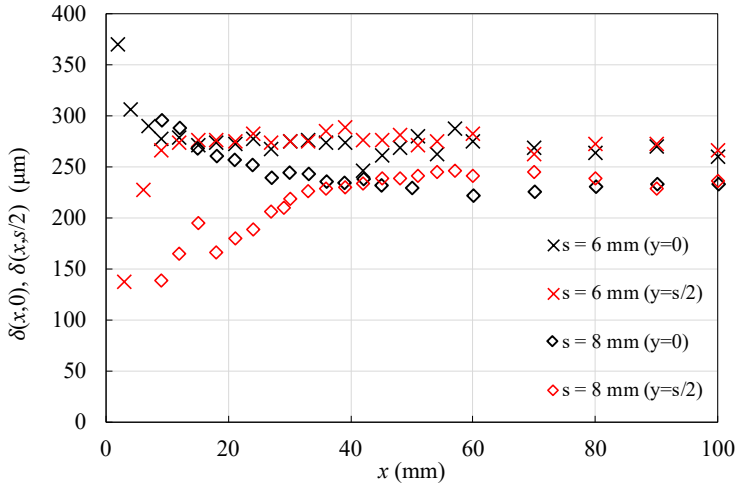

Figure S7. Streamwise film profile along $y = 0$ and $y = s/2$ for spacing $s = 6$ mm and 8 mm. Single row of perforations, Perforation diameter $d = 4$ mm, plate thickness $t = 1$ mm, and Reynolds number Re $= 38$ (curtain mode).

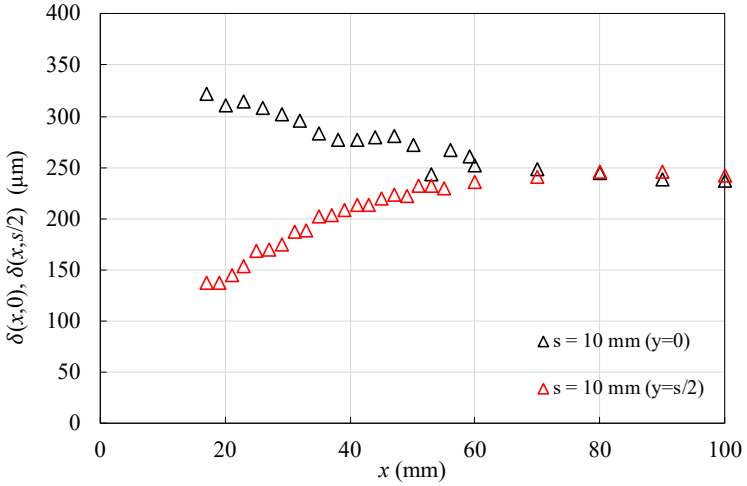

Figure S8. Streamwise film profile along $y = 0$ and $y = s/2$ for spacing $s = 10$ mm. Single row of perforations, Perforation diameter $d = 4$ mm, plate thickness $t = 1$ mm, and Reynolds number Re $= 38$ (curtain mode).

Figures S7 and S8 complete Figure 8 displayed in the main document and present the streamwise film profile along $y = 0$ and $y = s/2$ for $s = 6, 8, 10$ mm. $y = 0$ (resp. $y = s/2$) coincides with a crest (resp. a trough) of the free surface. Since the minimum measurable

thickness of the CCI sensor is about 100 µm, we cannot capture the beginning of the merging between two adjacent rivulets. Thus, at given spacing, merging starts at a distance slightly lower than the abscissa of the first measuring point along $y = s/2$. We observe that the film thickness along $y = 0$ (resp. $y = s/2$) decreases (resp. increases) with x and reaches a plateau. The smaller the spacing, the faster the plateau is reached and the higher is the plateau value.

A7. Liquid film pattern on a staggered array of perforations

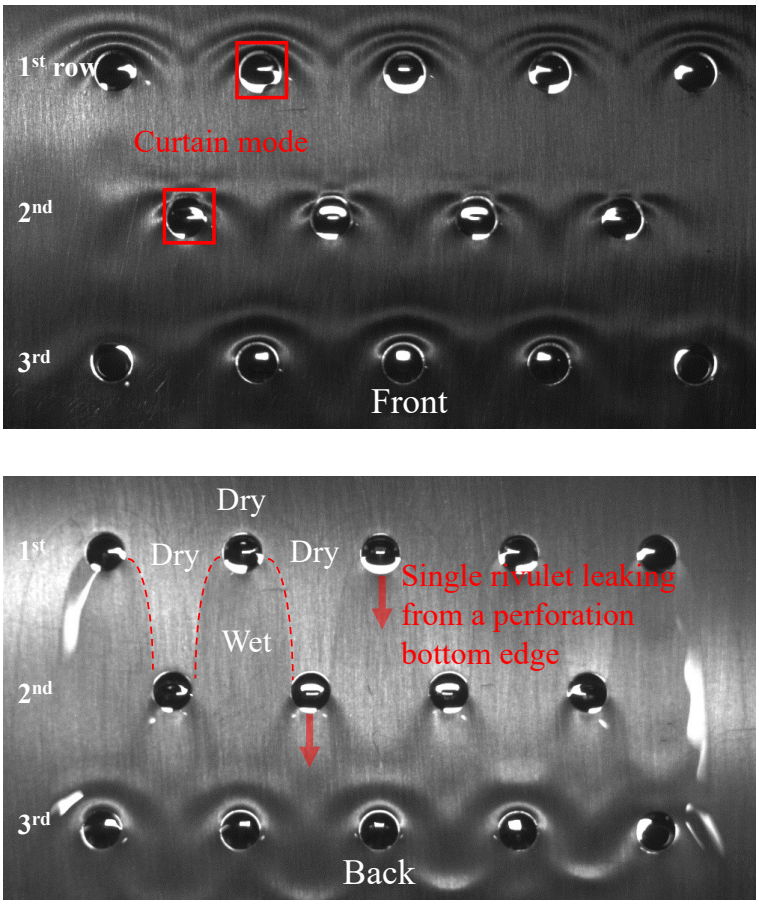

Figure S9. Liquid film pattern on a staggered array of perforations at Re $=$ 35 $\cong$ Re$_{cr}$ when all perforations are in curtain mode. Plate thickness t $=$ 1 mm, perforation diameter d $=$ 4 mm and spacing s $=$ 14 mm. (Top) Front of the plate (bottom) back of the plate.

Figure S9 and S10 show the flow pattern on a staggered array of perforation at Re$_{cr}$ and above. In that case, all the perforations (odd and even rows) operate in the curtain mode. The liquid leaks from the bottom edge of the perforations on the back of the plate. The corresponding rivulets widen as they flow in the x-direction. The liquid free surface is disturbed by waves traveling downstream. This phenomenon is clearly seen beneath the third row of perforations (Figure S10).

Figure S10. Liquid film pattern on a staggered array of perforations at Re $= 35 \cong \mathrm{Re}_{cr}$ when all perforations are in curtain mode. Plate thickness $t = 1$ mm, perforation diameter $d = 4$ mm and spacing $s = 14$ mm. Full view of the back of the plate.

A8. Derivation of the rivulet model and assessment of the assumptions

Following Shetty & Cerro[16], we fit the rivulet spanwise profiles with a Gaussian law:

$$\delta(x,y) = \delta_c(x) \exp\left(-\left(\frac{\left(y - y_c(x)\right)^2}{2\, m^2(x)}\right)\right) \quad (A1)$$

$\delta_c(x)$ is the maximum film thickness, $y_c(x)$ the spanwise location of the peak, and $m(x)$ the standard deviation of the Gaussian, which measures the lateral spreading of the rivulet. We determine these parameters for each spanwise profile (at given supply Reynolds number Re and given x) using the least-squares method. The parameter values of the best fits are reported in Table 2. The relative error is of the order of 1 to 2% for most of the fits, and it never exceeds 5%. We use $y_c(x)$ as a fitting parameter to improve the estimation of $\delta_c(x)$. However, since $y_c(x) \ll d$, we neglect the deviation of the peak from $y = 0$ in the further analysis.

Figure 11 shows that the spanwise profiles collapse into a single curve when $\delta(x,y)$ and y are appropriately rescaled. We deduce that the rivulet spanwise profiles are self-similar and well described by a Gaussian law. These results concord with the findings of Shetty and Cerro[16], who studied a rivulet draining down a vertical prewetted plate. We checked that the Gaussian law is a better approximation of the present rivulet profiles than the quartic similarity solution obtained by Duffy and Moffatt[27].

However, we remind that we could not measure the rivulet thickness close to the lateral contact line. Thus, the Gaussian law has only been validated against the core of the rivulet profile. We suppose hereafter that the Gaussian law holds over the whole rivulet spanwise profile. We will come back to this hypothesis later.

Q (L h^{-1})	Re	$x =$	2 mm	20 mm	40 mm	60 mm	80 mm	100 mm
20	24	δ_c (μm)	261	251	240	237	232	233
		y_c (mm)	-0.062	-0.004	0.119	-0.072	0.273	-0.005
		m (mm)	1.60	2.38	2.71	2.91	2.99	2.94
		Err (%)	1.5	1.7	1.4	2.0	2.1	2.1
24	29	δ_c (μm)	293	279	271	262	261	256
		y_c (mm)	-0.093	0.062	-0.057	0.249	0.121	0.219
		m (mm)	2.06	2.89	2.89	3.15	3.21	3.29
		Err (%)	2.0	1.9	2.1	1.4	3.9	2.2
28	33	δ_c (μm)	336	310	289	280	277	269
		y_c (mm)	0.061	0.152	0.405	0.160	0.245	0.479
		m (mm)	1.58	2.49	3.06	3.34	3.47	3.78
		Err (%)	1.4	1.9	2.6	2.3	3.1	2.9
32	38	δ_c (μm)	395	336	320	305	299	303
		y_c (mm)	0.014	0.233	-0.225	0.020	0.354	0.257
		m (mm)	1.66	2.68	2.75	3.84	3.76	4.06
		Err (%)	1.7	2.1	1.4	4.1	4.2	4.9
35	42	δ_c (μm)	416	347	330	325	306	299
		y_c (mm)	0.122	0.248	-0.101	0.114	0.264	-0.106
		m (mm)	1.50	2.73	3.15	3.29	3.79	4.07
		Err (%)	0.5	1.8	2.8	2.2	2.1	3.0

Table 2. Parameters of the Gaussian function that best fits the rivulet spanwise profile: δ_c, y_c and m as a function of the supply Reynolds number (Re) and streamwise location x, relative error (Err, L2-norm) between the experimental profile and the fitting curve.

To go further, we also assume that the velocity component in the x-direction is semi-parabolic (Nusselt profile):

$$u(x,y) = \frac{g}{2\nu}(2\,\delta(x,y)\,z\, - z^2) \quad (A2)$$

This assumption is reasonable if the rivulet is thin, its flow laminar, steady, and locally fully developed: data of Table 2 show that the rivulet thickness is at least one order of magnitude lower than its width, i.e., $\delta_c(x)/2m(x) \lesssim 0.1$. The upper bound of the rivulet Reynolds number Re_{rv} at the abscissa x equals $\mathrm{Re}_{rv} = \frac{1}{3}(\delta_c(x)/l_\nu)^3$ where $l_\nu = \nu^{2/3}/g^{1/3}$ is the visco-gravitational length. In the present dataset, the rivulet Reynolds number is systematically lower than $\mathrm{Re}_{rv} = 35$, the value reached at $x = 2$ mm for the supply Reynolds number $\mathrm{Re} = 42$. We expect that the flow is locally fully developed a few millimeters downstream of the perforation (see Appendix A9).

Then, the volume flow rate is given approximately by

$$q_t = \frac{g}{3\nu}\int_{-\infty}^{+\infty} \delta^3 dy \quad (A3)$$

or

$$q_t = \frac{g}{3\nu}\sqrt{\frac{2\pi}{3}}\,\delta_c^3(x)\,m(x) \quad (A4)$$

If this model is appropriate, the right-hand side of Eq. A4 calculated from the rivulet profile at the current abscissa x should be constant, i.e., independent on x. This quantity remains constant within a few percent along x, except close to the perforation (see Figure S11): the right-hand side of Eq. 4 estimated at $x = 2$ mm is up to 25% lower than the value calculated further downstream.

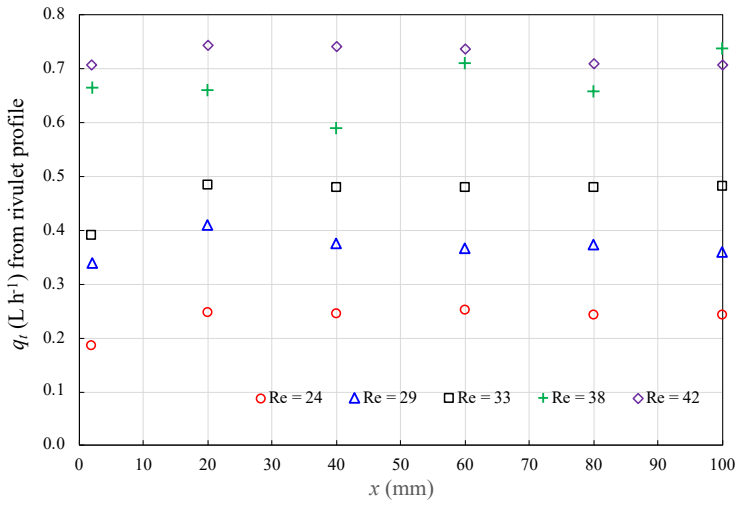

Figure S11. Transferred volume flow rate (q_t) as a function of the distance (x) from the perforation. q_t is estimated from Eq. A4 with the parameters of the rivulet spanwise profile.

We also compared the right-hand side of Eq. A4 to the transferred volume flow rate q_t measured experimentally. It appears that the former is significantly lower than the latter, i.e., from about 10% up to 35%. The discrepancy decreases as the supply Reynolds number increases. Two main reasons can be advanced. (i) As the supply Reynolds number decreases, the part of the rivulet cross-section satisfying $z > 100$ µm decreases. Then, the identification of the Gaussian parameters and the estimate of q_t from Eq. 4 become less reliable. (ii) The Gaussian law fails to describe the region of the rivulet close to the lateral contact line because the liquid contact angle on the plate is low but not equal to zero as in Shetty & Cerro's experiments, where the plate was prewetted. We retain that the product $\delta_c^3(x)\, m(x)$ is approximately constant for $x \geq x_0$.

If the flow is viscous and $1 \gg |\partial\delta/\partial y| \gg |\partial\delta/\partial x|$, the rivulet thickness satisfies the thin-film equation given by Duffy & Moffatt[27]. This equation reads for a steady rivulet flowing down a vertical plate:

$$\delta \frac{\partial^4 \delta}{\partial y^4} + 3 \frac{\partial \delta}{\partial y} \frac{\partial^3 \delta}{\partial y^3} + 3 \frac{\rho g}{\sigma} \frac{\partial \delta}{\partial x} = 0 \quad (A5)$$

We must be careful: the Reynolds number of the rivulet is small but the flow is not strictly viscous in our experiments. The conditions on the thickness derivatives are fulfilled. $\partial\delta/\partial y$ is of the order of $\delta_c(x)/m(x)$ which is much smaller than 1 for $x \gtrsim 20-40$ mm. The ratio of $\partial\delta/\partial x$ to $\partial\delta/\partial y$ is of the order of $m(x)/x$ which is much lower than 1 for $x \gtrsim 20-40$ mm (see Table 2).

We now restrict our analysis to $y = 0$, where the rivulet peaks, and assume a Gaussian spanwise profile centered at $y = 0$ (Eq. 1 with $y_c(x) = 0$). Then, Eq. A5 becomes:

$$\frac{d\delta_c}{dx} + \frac{\sigma}{\rho g}\frac{\delta_c^2}{m^4} = 0 \quad (A6)$$

We further proceed as Shetty & Cerro[16] to get the scaling law followed by δ_c and m. We have just seen that the quantity $\delta_c^3(x)m(x)$ remains constant along x if x is large enough. We note x_0 the first measuring point where $\delta_c^3(x)m(x)$ reaches this plateau value (see Figure S11). $x_0 =$ 20 mm for Re = 24, 29, 33 and $x_0 = 2$ mm for Re = 38, 42. For $x > x_0$, let

$$c_1 = 2\left(\delta_c^3(x)m(x)\right)^2 \quad (A7)$$

and replace in Eq. A6:

$$\frac{d\delta_c}{dx} + \frac{4\sigma}{c_1^2\rho g}\delta_c^{14} = 0 \quad (A8)$$

The streamwise coordinate (x), the maximum thickness (δ_c), and the standard deviation of the Gaussian (m) are rescaled as follows:

$$x^{\#} = \frac{x - x_0}{2m(x_0)} \quad ; \quad \delta_c^{\#}(x) = \frac{\delta_c(x)}{\delta_c(x_0)} \quad ; \quad m^{\#}(x) = \frac{m(x)}{m(x_0)}$$

Then, Eq. A8 is recast as:

$$\frac{d\delta_c^{\#}}{dx^{\#}} + \frac{16\alpha^3}{3\,\mathrm{Ca}}(\delta_c^{\#})^{14} = 0 \quad (A9)$$

α and Ca are the aspect ratio and capillary number of the rivulet at $x = x_0$:

$$\alpha = \frac{\delta_c(x_0)}{2m(x_0)} \quad ; \quad \mathrm{Ca} = \frac{\mu}{\sigma}\left(\frac{g\delta_c^2(x_0)}{3\nu}\right)$$

The integration of Eq. A8 from $x^{\#} = 0$ to an arbitrary value of $x^{\#}$ gives[16]:

$$\delta_c^{\#}(x^{\#}) = \left(1 + \frac{208}{3}\frac{\alpha^3}{\mathrm{Ca}}x^{\#}\right)^{-1/13} \qquad (A10)$$

By combining Eq. 7 and 10, we get the evolution of the rescaled rivulet width:

$$m^{\#}(x) = \left(1 + \frac{208}{3}\frac{\alpha^3}{\mathrm{Ca}}x^{\#}\right)^{3/13} \qquad (A11)$$

Since the quantity $2\left(\delta_c^3(x)m(x)\right)^2$ is not strictly conserved experimentally (even for $x > x_0$) and slightly fluctuates along x, it is relevant to distinguish between the "best" estimate of c_1 taken as the mean value of $2\left(\delta_c^3(x)m(x)\right)^2$ over the region $x > x_0$ and denoted $\bar{c}_1$, and the value of $2\left(\delta_c^3(x)m(x)\right)^2$ at $x = x_0$, i.e., $c_0 = 2\left(\delta_c^3(x_0)m(x_0)\right)^2$. The former appears when deriving Eq. A8 from Eq. A6 and Eq. A7. The latter appears when rescaling Eq. A9. Then, the argument of the power-laws (Eq. A10-A11) should be transformed as follows:

$$\left(1 + \frac{208}{3}\frac{\alpha^3}{\mathrm{Ca}}x^{\#}\right) \rightarrow \left(1 + \frac{208}{3}\frac{\alpha^3}{\mathrm{Ca}}\beta x^{\#}\right) \qquad (A12)$$

with $\beta = \left(\frac{c_0}{\bar{c}_1}\right)^2$.

A9. Length required for a rivulet flow to be locally fully developed

Let us estimate the length required for the rivulet flow to be locally fully developed. We consider the rivulet peak thickness at the first measuring point downstream of the perforation: $\delta_c(x = 2\text{mm})$ ranges between 261µm to 416 µm (see Table 2). An estimate of the fluid mean velocity (U) on the rivulet centerline is given by:

$$U \cong \frac{g\,\delta_c^2}{3\nu}$$

The length to establish a Poiseuille flow between two parallel plates reads†:

$$\frac{L_m}{D_h} = 0.3125 + 0.011 \times \mathrm{Re}_{Dh}$$

where D_h is the hydraulic diameter. $D_h = 2H$ for two parallel plates spaced a distance H apart. We then deduce the length required for the rivulet flow to be locally fully developed:

$$\frac{L_m}{\delta_c} \cong 1.25 + 0.044\frac{U\delta_c}{\nu}$$

We find that L_m ranges from 0.7 mm to 3 mm when the supply flow rate on the front of the plate varies between $Q = 20$ L h^{-1} and $Q = 35$ L h^{-1}, respectively.

† Atkinson B, Brocklebank MP, Card CCH, Smith JM. Low Reynolds number developing flows. *AIChE Journal*. 1969;15:548-553.

A10. Scaling law of the rivulet merging

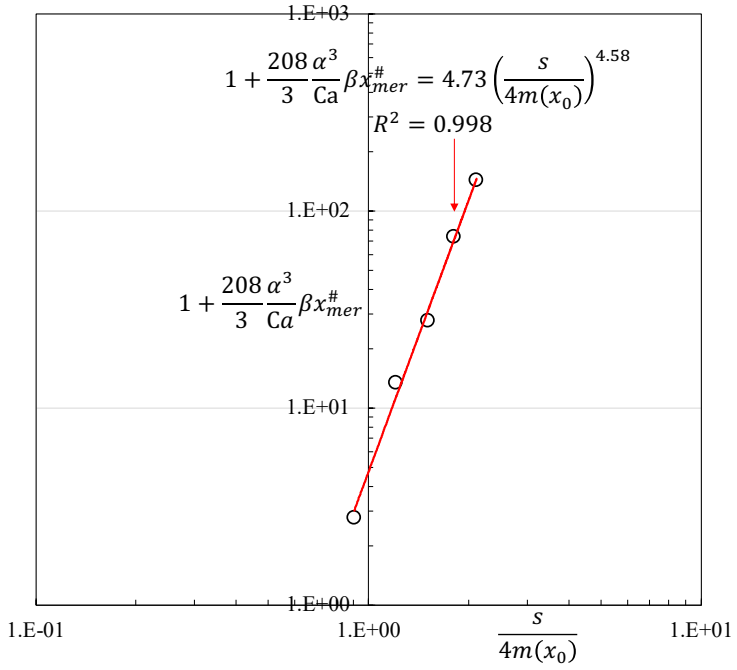

Figure S12. Rescaled distance between the onset of rivulet merging and the row of perforations as a function of the rescaled perforation spacing. $d = 4$ mm, $t = 1$ mm, Re $= 38$ and $s = 6$, 8, 10, 12, 14 mm. Data points are fitted by a power law (red solid line) using the least-squares method.

Figure S12 presents the variations of **r**escaled distance required for rivulet merging ($1+\frac{208}{3}\frac{\alpha^3}{\mathrm{Ca}}\beta x_{mer}^{\#}$) as a function of the rescaled perforation spacing ($s/\left(4m(x_0)\right)$). The data points are fitted by a power law using the least-squares method. The exponent (4.58) is close to the theoretical value ($13/3 = 4.33$). The prefactor (4.73) is significantly greater than the expected value (1). We presently overestimate $x_{mer}^{\#}$ because the first measuring point (corresponding to a film thickness close to 100 µm) used to estimate the onset of merging is systematically located downstream of the actual position where the rivulets start to merge (corresponding to a vanishing film thickness).

A11. Model of liquid transfer through a staggered array of perforations

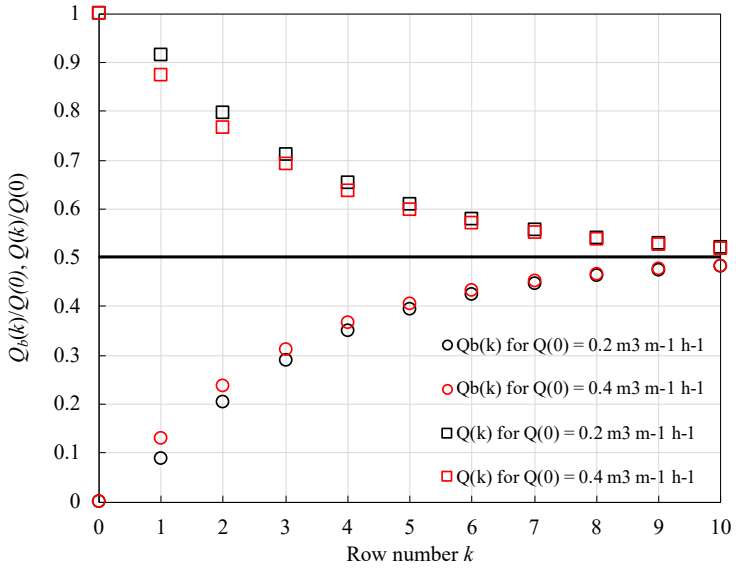

Figure S13. Rescaled volume flow rate per unit width on the back ($Q_b(k)$) and on the front ($Q(k)$) of the plate as a function of the row number (k): results provided by the model for $d =$ 4 mm, $t = 1$ mm, $s = 14$ mm, $Q = 0.2$ m^3 m^{-1} h^{-1} and $Q = 0.4$ m^3 m^{-1} h^{-1}.

Figure S13 shows the variations of the volume flow rate per unit width along the front and the back of the perforated plate computed from our simple recurrence model. It appears that the volume flow rates on the front and the back of the plate tend to equalize as the row number (k) increases. The asymptotic value is equal to half the supply flow rate. The transferred volume flow rate decreases with k since the driving force ($Q(k-1) - Q_b(k-1)$) decreases. Q_b reaches 90% of its asymptotic value ($Q(0)/2$) beneath the 7th row of perforations.

The solutions computed for $Q = 0.2$ m^3 m^{-1} h^{-1} and $Q = 0.4$ m^3 m^{-1} h^{-1} are not proportional since Eq. 18 describing the liquid transfer through the first row of perforations contains a constant term, i.e., the threshold flow rate $Q_{th} = 0.1$ m^3 m^{-1} h^{-1}. Then, the points associated with $Q = 0.2$ m^3 m^{-1} h^{-1} and $Q = 0.4$ m^3 m^{-1} h^{-1} do not superimpose. However, if $Q_{th} = 0$, the pointset would be unique.

For $Q(0) = 0.4$ m^3 m^{-1} h^{-1}, we expect that $Q_b(k)$ and $Q(k)$ relax even more rapidly to their asymptotic value ($Q(0)/2$) than the predictions of Figure S13. Indeed, experiments show that the liquid transfer through the perforations is enhanced when the supply flow rate ($Q(0)$) increases (see Figure 10).